Neurobiology of Disease

Ndnf Interneuron Excitability Is Spared in a Mouse Model of Dravet Syndrome

Sophie R. Liebergall[1,2,3] **and Ethan M. Goldberg**[1,2,4,5,6]

[1]Department of Neuroscience, [2]Neuroscience Graduate Group, [3]Medical Scientist Training Program, and [4]Neurology, The University of Pennsylvania Perelman School of Medicine, Philadelphia, Pennsylvania 19104, [5]The Epilepsy Neurogenetics Initiative and [6]Division of Neurology, The Children's Hospital of Philadelphia, Philadelphia, Pennsylvania 19104

Dravet syndrome (DS) is a neurodevelopmental disorder characterized by epilepsy, developmental delay/intellectual disability, and features of autism spectrum disorder, caused by heterozygous loss-of-function variants in *SCN1A* encoding the voltage-gated sodium channel α subunit Nav1.1. The dominant model of DS pathogenesis is the "interneuron hypothesis," whereby GABAergic interneurons (INs) express and preferentially rely on Nav1.1-containing sodium channels for action potential (AP) generation. This has been shown for three of the major subclasses of cerebral cortex GABAergic INs: those expressing parvalbumin (PV), somatostatin, and vasoactive intestinal peptide. Here, we define the function of a fourth major subclass of INs expressing neuron-derived neurotrophic factor (Ndnf) in male and female DS (*Scn1a*+/−) mice. Patch-clamp electrophysiological recordings of Ndnf-INs in brain slices from *Scn1a*+/â mice and WT controls reveal normal intrinsic membrane properties, properties of AP generation and repetitive firing, and synaptic transmission across development. Immunohistochemistry shows that Nav1.1 is strongly expressed at the axon initial segment (AIS) of PV-expressing INs but is absent at the Ndnf-IN AIS. In vivo two-photon calcium imaging demonstrates that Ndnf-INs in *Scn1a*+/â mice are recruited similarly to WT controls during arousal. These results suggest that Ndnf-INs are the only major IN subclass that does not prominently rely on Nav1.1 for AP generation and thus retain their excitability in DS. The discovery of a major IN subclass with preserved function in the *Scn1a*+/â mouse model adds further complexity to the "interneuron hypothesis" and highlights the importance of considering cell-type heterogeneity when investigating mechanisms underlying neurodevelopmental disorders.

Key words: **Dravet syndrome; interneurons; Nav1.1; Ndnf; neurogliaform; *SCN1A***

Significance Statement

Dravet syndrome (DS) is a severe neurodevelopmental disorder characterized by epilepsy, developmental impairment, and autism spectrum disorder, due to mutations in the gene *SCN1A* encoding the voltage-gated sodium channel subunit Nav1.1. Prior work has demonstrated impaired spike generation across subtypes of GABAergic cerebral cortex inhibitory interneurons (INs) in DS mouse models due to the prominent expression of Nav1.1 in INs versus excitatory principal cells. Here, we show that a previously unexamined interneuron subtype—neocortical Layer 1 INs expressing neuron-derived neurotrophic factor—is unique among INs in that they do not express Nav1.1 and exhibit normal electrical excitability in a mouse model of DS. This work highlights the complex cellular and circuit mechanisms underlying the pathogenesis of this neurodevelopmental disorder.

Introduction

Dravet syndrome (DS) is a neurodevelopmental disorder characterized by treatment-resistant epilepsy and developmental delay/intellectual disability with features of autism spectrum disorder (ASD) (Dravet, 2011). DS is caused by heterozygous loss-of-function variants in *SCN1A* encoding the voltage-gated sodium (Na^+) channel α subunit Nav1.1 (Claes et al., 2001). The leading hypothesis of DS pathophysiology states that Nav1.1 is preferentially expressed in cerebral cortex GABAergic interneurons (INs); therefore, loss of Nav1.1 causes selective IN

Received Oct. 15, 2023; revised Jan. 10, 2024; accepted Jan. 30, 2024.

Author contributions: S.R.L. and E.M.G. designed research; S.R.L. performed research; S.R.L. analyzed data; S.R.L. and E.M.G. wrote the paper.

This work was supported by the National Institutes of Health Grants F31NS132519 to S.R.L. and R01NS119977 to E.M.G. as well as a research grant from the Sonja Matos Foundation for Biophysical Study to E.M.G. We thank Emily Hoddeson and Xiaohong Zhang for technical assistance with mouse colony management, Damaris Lorenzo for the gift from the anti-Ankyrin-G antibody, Karl Deisseroth for the distribution of pAAV-Ef1a-fDIO-mCherry, and Douglas Kim and the GENIE project for the distribution of pGP-AAV-hSyn-FLEX-GCaMP7s.

The authors declare no competing financial interests.

Correspondence should be addressed to Ethan M. Goldberg at goldberge@chop.edu.

https://doi.org/10.1523/JNEUROSCI.1977-23.2024

impairment leading to circuit dysfunction (Yu et al., 2006; Tai et al., 2014). INs are a heterogenous population that can be divided into subclasses based on molecular markers correlated with electrophysiological, morphological, and anatomical properties (Tremblay et al., 2016). Previous studies in *Scn1a*+/− mouse models have demonstrated dysfunctional action potential (AP) generation in neocortical parvalbumin (PV), somatostatin (SST), and vasoactive intestinal peptide (VIP)-expressing INs as well as impairment at PV-IN:pyramidal cell synapses, yet how this subclass-specific dysfunction leads to the complex phenotype of DS remains unclear (Ogiwara et al., 2007; Tai et al., 2014; Goff and Goldberg, 2019; Kaneko et al., 2022). There is, however, a fourth major subclass of neocortical INs—those expressing neuron-derived neurotrophic factor (Ndnf)—the functional status of which is unknown in DS.

Ndnf has been identified as a marker of the majority of the understudied IN population residing in Layer 1 of the neocortex (Tasic et al., 2016; Gouwens et al., 2020). Ndnf-INs can be divided into two subpopulations—neurogliaform cells (NGFCs) and Canopy cells—based on electrophysiologic and morphologic properties that correlate with neuropeptide Y expression (Schuman et al., 2021). NGFCs were first identified by Ramon y Cajal on the basis of a dense local axonal plexus (Ramon y Cajal, 1922), and they display a characteristic late spike at near-rheobase depolarizations with nonadapting spike trains at higher current injections (Kawaguchi, 1995). These cells also have unique synaptic properties including "volume transmission" that activates both $GABA_A$ and $GABA_B$ receptors on target pyramidal cells and PV-INs (Tamás et al., 2003; Zhu and Zhu, 2004; Wozny and Williams, 2011; Jiang et al., 2013; Muralidhar et al., 2014) as well as extensive electrical connectivity (Oláh, 2007). Additionally, NGFCs release nitric oxide and insulin, suggesting a role in neurovascular coupling and regulation of cellular metabolism (Cauli et al., 2004; Cauli, 2010; Molnár et al., 2014; Csajbók et al., 2019). In contrast, Canopy cells fire at stimulus onset and have a less dense axonal arbor confined to the upper half of Layer 1 (Schuman et al., 2021). The main synaptic targets of Canopy cells are unknown and they form only sparse and weak synapses on Layer 2/3 pyramidal cells (Schuman et al., 2019). Ndnf-INs have been shown to gate long-range thalamocortical feedback loops, modulate the gain of sensory inputs, decouple hippocampal pyramidal cells from gamma oscillations, and play a role in associative learning (Abs et al., 2018; Anastasiades et al., 2021; Cohen-Kashi Malina et al., 2021; Hay et al., 2021). Though recent work has begun to emphasize the importance of Ndnf-INs in normal brain function, Ndnf-IN function/dysfunction within pathological cortical microcircuits remains unexamined.

Here, we perform a comprehensive assessment of Ndnf-IN intrinsic excitability, synaptic transmission, and in vivo activity in male and female *Scn1a*+/− mice relative to WT age- and sex-matched littermate controls. *Scn1a*+/− Ndnf-INs do not show impaired AP generation or repetitive firing relative to WT across development, suggesting that Ndnf-IN intrinsic excitability does not substantially depend on Nav1.1. This hypothesis is supported by the lack of Nav1.1 immunohistochemical signal at the Ndnf-IN axon initial segment (AIS) and preserved somatic Na^+ current density in *Scn1a*+/− Ndnf-INs. Furthermore, Ndnf-IN cortical microcircuit function does not appear to be impaired in DS, as there are no changes in the amplitude or kinetics of *Scn1a*+/− Ndnf-IN–mediated unitary postsynaptic currents, and *Scn1a*+/− Ndnf-INs were similarly recruited during arousal state transitions in vivo. Our work identifies Ndnf-INs as a major IN subclass that does not significantly rely on Nav1.1 and thus displays intact excitability across development in *Scn1a*+/− mice.

Materials and Methods

Experimental animals. All procedures and experiments were approved by the Institutional Animal Care and Use Committee at the Children's Hospital of Philadelphia and were conducted in accordance with the ethical guidelines of the National Institutes of Health. All studies used both male and female mice in equal proportions. After weaning at P21, mice were group-housed with up to five mice per cage and maintained on a 12 h light/dark cycle with *ad libitum* access to food and water. Mouse strains used in this study included *Scn1a*+/− mice on a 129S6.SvEvTac background (RRID: MMRRC_037107-JAX) generated by a targeted deletion of exon 1 of the *Scn1a* gene, Ndnf-Flp mice (B6(Cg)-Ndnftm1.1(flpo)Ispgl/J; RRID: IMSR_JAX:034876), Ndnf-Cre mice (Ndnftm1.1(cre)Rudy/J; RRID: IMSR_JAX:030757), PV-Cre mice (B6.129P2-Pvalbtm1(cre)Arbr/J; RRID: IMSR_JAX:017320), and Ai14 (tdT) mice (B6.Cg-Gt(ROSA)26Sortm14(CAG-tdTomato)Hze/J; RRID: IMSR_JAX:007914).

Homozygous Ndnf-Flp or Ndnf-Cre mice were crossed to heterozygous *Scn1a*+/− mice to generate *Scn1a*.Ndnf-Flp or *Scn1a*.Ndnf-Cre mice and WT littermate controls. All mice used for experiments were maintained on a near 50:50 129S6:C57/BL6J background to reproduce the core DS endophenotypes in *Scn1a*+/− mice (Miller et al., 2014; Mistry et al., 2014). The genotypes of all mice were determined via PCR of tail snips obtained at P7. 100% (6/6) of P20 *Scn1a*.Ndnf-Flp mice, and 0% (0/5) of WT.Ndnf-Flp mice exhibited temperature-sensitive seizures at or below 42°C core body temperature, supporting the validity of using these mice as a model of DS.

Adeno-associated virus injections and cranial window implantation. For slice electrophysiology experiments, WT.Ndnf-Flp and *Scn1a*+/-.Ndnf-Flp mice were injected at P0–2 with pAAV-Ef1a-fDIO-mCherry as described previously (Kim et al., 2013) to facilitate recording at the P16–21 developmental timepoint. Briefly, P0–2 mice were anesthetized on ice and then injected through the skull with 0.75 µl of AAV9 in each hemisphere. Ndnf-Flp mice were used for slice electrophysiology experiments because this line demonstrated significantly less nonspecific labeling following P0–2 adeno-associated virus (AAV) injection relative to Ndnf-Cre mice. For 2P imaging experiments, WT.Ndnf-Cre and *Scn1a*.Ndnf-Cre mice age >P35 were anesthetized with isoflurane (induction, 3–4%; maintenance, 1–1.5%), and body temperature and respiration were continuously monitored. A craniotomy 3 mm craniotomy located 1 mm posterior and 3 mm lateral to the bregma was made, and 4 × 60 nl injections of virus (AAV9-pGP-AAV-syn-FLEX-jGCaMP7s-WPRE diluted to a titer of 5e12 in sterile PBS) were made at a depth of 300 µm and a rate of 1 nl/min using a 50 µm diameter beveled tip glass pipette with a Nanoject III (Drummond Scientific). Following virus injection, a 3 mm circular coverslip glued to a 5 mm circular coverslip was affixed in place to cover the craniotomy, and a custom stainless steel headbar was cemented to the skull. Mice were given buprenorphine-SR 0.5 mg/kg, cefazolin 500 mg/kg, and dexamethasone 5 mg/kg perioperatively and monitored for recovery and infection for 48 h following surgery.

Acute slice preparation. Acute slices were prepared as previously described (Goff and Goldberg, 2019). Briefly, mice were anesthetized with isoflurane, and the brain was transferred to ice-cold artificial cerebral spinal fluid (ACSF) containing (in mM) 87 NaCl, 75 sucrose; 2.5 KCl, 1.0 $CaCl_2$, 2.0 $MgSO_4$, 26 $NaHCO_3$, 1.25 NaH_2PO_4, and 10 glucose, equilibrated with 95% O_2 and 5% CO_2, and sliced at a thickness of 300 µm using a Leica VT-1200S vibratome. Slices were allowed to recover in ACSF for 30 min at 32°C and then maintained at room temperature (RT) for up to 6 h before recording. In preparation for recording, slices were transferred to a chamber under an Olympus BX61 microscope and continuously perfused at a rate of 3 ml/min and temperature of 32°C with a recording solution that contained the following (in mM): 125 NaCl, 2.5 KCl, 2.0 CaCl, 1.0 MgSO, 26 NaHCO, 1.25 NaH_2PO, and 10 glucose.

Whole-cell acute brain slice recordings. Ndnf-INs were identified by mCherry expression visualized with epifluorescence. Whole-cell recordings were obtained from Layer 1 primary somatosensory cortex (S1;

"barrel") with 1–3 cells recorded from each slice in either single or paired configuration. Patch pipettes with a resistance of 4–6 MΩ were pulled from borosilicate glass using a P-97 puller (Sutter Instruments). For whole-cell recordings of intrinsic properties, pipettes were filled with intracellular solution containing the following (in mM): 130 K-gluconate, 6.3 KCl, 0.5 EGTA, 1.0 $MgCl_2$, 10 HEPES, 4.0 Mg-ATP, and 0.3 Na-GTP; pH was adjusted to 7.30 with KOH and osmolarity to 290 mOsm. For paired recordings of synaptic transmission, pipettes were filled with intracellular solution containing the following (in mM): 126 K-gluconate, 4 KCl, 10 HEPES, 4.0 Mg-ATP, 0.3 Na-GTP, and 10 Na_2-phosphocreatine; pH was adjusted to 7.30 with KOH and osmolarity to 290 mOsm. Signals were sampled at 100 kHz with a MultiClamp 700B amplifier (Molecular Devices), filtered at 10 kHz, digitized using a DigiData 1550A, and acquired using pClamp10 software. Recordings were discarded if the cell had a resting membrane potential greater than −50 mV, or if access resistance was >30 MΩ and/or increased by >20% during the recording. We did not correct for liquid junction potential.

Electrophysiological data analysis. We performed an analysis of intrinsic properties and paired recordings blind to genotype using custom MATLAB (MathWorks) code with quality control using a manual confirmation in Clampfit (pCLAMP). Resting membrane potential (V_m) was calculated as the average value of a 600 ms window with no direct current injection. Input resistance (R_m) was calculated using the average response to a −60 pA hyperpolarizing current injection using Ohm's law ($R_m = \Delta V/I$). AP threshold was calculated as the value at which the derivative of the voltage (dV/dt) first reached 20 mV/ms. Spike height was calculated as the absolute maximum voltage value of a given AP. Spike amplitude was calculated as the difference between spike height and AP threshold. AP rise time was calculated as the time from the AP threshold to the absolute maximum voltage of the AP. AP half-width was defined as the width of the AP (in ms) at half-maximal amplitude. AP afterhyperpolarization (AHP) amplitude was calculated as the difference between the minimum voltage value of the AHP and the AP threshold voltage. Quantification of single spike properties was done using the first AP during the first current injection that elicited >10 APs. This sweep was chosen to ensure that the analyzed AP always occurred at the onset of the current injection to control for the variability in the latency to the first spike in near-rheobase current injections in NGFCs (which influences properties such as AP threshold and rise time). Rheobase was defined as the minimum current injection that elicited an AP using a 600 ms sweep at 20 pA intervals. The maximal instantaneous firing was calculated using the smallest interspike interval elicited during the current step protocol. Maximal steady-state firing was defined as the maximal mean firing frequency (FF) with a minimum requirement for a spike being the presence of a measurable AP threshold and the voltage overshooting 0 mV.

For statistical testing of equivalence, the following values were proposed as the upper and lower equivalence bounds of each property based on reported impairments in PV-INs (Favero et al., 2018; Goff and Goldberg, 2019): V_m, ±10 mV; R_m, ±100 mOhms; time constant, ±50 ms; rheobase, ±100 pA; AP threshold, ±5 mV; AP rise time, ±0.1 ms; max rise slope, ±100 mV/ms; AP half-width, ±0.16 ms; AP peak, ±10 mV; AP amplitude, ±10 mV; AHP amplitude, ±10 mV; sag ratio, ±1%; APs at rheobase, ±5; maximal instantaneous FF, ±116 Hz; maximal steady-state FF, ±97 Hz; FF at 2× rheobase, ±100 Hz; and latency to first spike, ±100 ms.

For paired recordings of unitary synaptic transmission, 10 sweeps were aligned to the peak of the AP in the presynaptic cell and averaged. The inhibitory postsynaptic current (IPSC) amplitude was defined as the difference between the average current of 100 ms before the peak of the presynaptic AP and the maximum current value after the presynaptic AP. Time to peak was defined as the time between the peak of the presynaptic AP and the peak of the IPSC. The threshold for a pair to be considered successfully connected was an IPSC with an amplitude exceeding four times the standard deviation of the noise.

Ndnf-IN subpopulation classification. Ndnf-INs were classified as either NGFCs or Canopy cells as defined by Schuman et al. (2019), based on near-rheobase firing patterns obtained via current-clamp recordings of intrinsic properties. Cells were classified as NGFCs if the latency to the first spike at a rheobase current injection was greater than 50 ms. Because NGFCs may only exhibit late spiking within a narrow range of current injections, current steps were repeated in 5 pA increments near rheobase to confirm the presence/absence of delayed spiking versus subthreshold passive depolarization "hump" to confirm that a cell was indeed an NGFC or a Canopy cell.

Immunohistochemistry. Mice were anesthetized with isoflurane and transcardially perfused with 0.1 M PBS followed by 1% paraformaldehyde in 0.1 M PBS. Brains were postfixed in 1% paraformaldehyde overnight at 4°C and cut into 40 µm sections using a Leica VT-1200S vibratome. The slices were permeabilized with 0.3% Triton X-100 (Sigma-Aldrich) for 30 min at RT and then blocked in 5% bovine serum albumin (BSA, Sigma-Aldrich) in PBS for 1 h at RT. We stained with primary antibodies overnight at 4°C in PBS with 5% BSA and 0.1% Triton X-100. Primary antibodies used included mouse anti-Nav1.1 (NeuroMab K74/71, 1:500), as well as rabbit anti-Ankyrin-G (1:500) which was generated in the Bennett lab and is previously described (Lorenzo et al., 2019; Cousin et al., 2021). The following day, the slices were washed with PBS and stained with Alexa Fluor 488–conjugated goat anti-mouse IgG1 (Molecular Probes, 1:500) and Alexa Fluor 405–conjugated goat anti-rabbit IgG (Molecular Probes, 1:500) secondary antibodies in PBS with 5% BSA and 0.1% Triton X-100. After washing, the slides were coverslipped and sealed with PVA-DABCO (Sigma-Aldrich).

Z-stack images of either Ndnf- or PV-INs were captured on a Leica TCS SP8 confocal microscope using a 40× oil immersion objective with 4× digital zoom. Only cells with intact AISs, as determined by Ankyrin-G staining, were included in the analysis. Quantification of Nav1.1 staining at the AIS was performed using the ImageJ SNT plug-in and custom MATLAB code (Schindelin et al., 2012; Arshadi et al., 2021). First, the AIS, as defined by Ankyrin-G staining, was manually traced in three dimensions using SNT. Next, the background fluorescence, defined as the mean fluorescence intensity of each slice, was subtracted from the Nav1.1 channel fluorescence intensity of each slice. Then, the SNT tracing was used to define a 1 µM diameter mask of the AIS, and the Nav1.1 channel fluorescence values within this mask were extracted and plotted.

Nucleated macropatch slice recordings. Nucleated macropatch recordings of Na^+ currents were performed as described previously (Tamagnini, 2021). Briefly, acute slices were prepared for current-clamp recordings, then transferred to a recording chamber, and continuously perfused at a rate of 3 ml/min and temperature of 32°C with a recording solution that contained the following (in mM): 125 NaCl, 2.5 KCl, 2.0 $CaCl_2$, 1.0 $MgSO_4$, 26 $NaHCO_3$, 1.25 NaH_2PO_4, and 10 glucose. In some recordings, 5 mM 4-aminopyridine (4-AP) and 10 mM tetraethylammonium (TEA) were added to the recording solution to more completely block K^+ channels. Four to six MΩ patch pipettes were filled with intracellular solution containing the following (in mM): 140 CsFl, 1.0 EGTA, 2.0 $MgCl_2$, 10 HEPES, 4.0 Na_2-ATP, and 0.3 Na_2-GTP; pH was adjusted to 7.30 with NaOH, and osmolarity was adjusted to 290 mOsm. After a cell was patched in the whole-cell configuration, negative pressure was applied while the pipette was withdrawn axially until visual confirmation of the formation of a nucleated macropatch was achieved. Macropatches were completely removed from the brain slice for recording. Currents were sampled at 33 kHz with a MultiClamp 700B amplifier (Molecular Devices), filtered at 10 kHz, digitized using a DigiData 1550A, and acquired using pClamp10 software. All recordings had an access resistance of <20 MΩ. Macropatch capacitance (generally 1–3 pF) was estimated in response to a pulse of −50 mV and was compensated. Recordings of Na^+ channel activation were performed by steps from a holding potential of −100 mV to test potentials between −80 and +60 mV in 5 mV increments for 30 ms at 0.5 Hz. Leak currents were digitally subtracted online using a P/4 procedure.

In vivo *pupillometry, locomotion tracking, and 2P calcium imaging.* Three weeks after the cranial window surgery, mice were habituated to head fixation in a custom chamber with transparent siding floating on

a Mobile HomeCage (Neurotar) for a 20 min daily session for 5 d or until the mouse showed spontaneous running bouts and the absence of escape or freezing behaviors. Airflow into the Mobile HomeCage stage provided ~40–45 db pink noise during the experiment, and locomotion speed was tracked by the Mobile HomeCage locomotion tracking software (Neurotar). An infrared (IR) 850 nm light source and IR CCD camera (Grasshopper 3, Teledyne FLIR) were positioned 15 cm away from the ipsilateral eye to acquire pupillometry videos at 100 Hz. Neural and behavioral data were synchronized by a transistor-transistor logic pulse at the start and end of each recording session.

2P imaging was performed on an Ultima 2Pplus microscope (Bruker) equipped with a resonant scanner (Cambridge Technology) using a tunable femtosecond-pulsed IR InSight X3 laser (Spectra-Physics) with output controlled by a Pockels cell (Conoptics). GcaMP7s signal was imaged at 950 nm at 30 Hz with a gallium arsenide phosphide photodetector (H7422-40, Hamamatsu) using a 16/0.8 NA water immersion objective (Nikon) and an additional 2× optical zoom. Ten minute recordings were performed across 4–5 distinct fields of view in each mouse over two recording sessions.

Pupillometry data analysis. Pupillometry analysis was performed as described in Goff et al. (2023). Briefly, we trained a DeepLabCut network on a Windows system equipped with an Nvidia RTX A5000 GPU by first extracting 10 frames per animal using the *k*-means algorithm and manually labeling four markers identifying the bounds of the pupil. Then we trained the network on this training data using the ResNet-50 pretrained model (with default parameters) for 300,000 iterations. The network was evaluated for accuracy and generalization. Pupil marker locations were output from DLC as a csv file. Custom MATLAB code was used to calculate the pupil diameter by averaging the Euclidean distance between the north/south and east/west points. Blinks were removed from the data set using a median filter (500 ms window) and replaced through linear interpolation.

Analysis of in vivo *neural activity.* Cell detection and extraction of neuronal activity were performed as previously described (Goff et al., 2023). Briefly, we used the Suite2p package to perform a nonrigid registration, detection of cell ROIs, and extraction of fluorescence values from ROIs (Pachitariu et al., 2016). A blinded experimenter manually performed quality control on all potential cell ROIs. For each ROI, the neuropil signal extending 30 µm from each ROI (excluding any other detected ROIs) was subtracted from the fluorescence values within the ROI. Fluorescence values in all figures are reported as $\frac{dF(t)}{F_0} = \frac{F(t)-F_0}{F_0}$, where F_0 is the 10th percentile of each neuron's fluorescence trace, adjusted by using a linear interpolation between the average F_0 values for the first and second halves of the recording.

Correlations between neural activity and pupil diameter, and between neural activity and locomotion speed, as well as cell–cell correlations (between all pairs of cells within a single FOV), were described using a zero-lag Pearson's correlation coefficient (r_n). Shuffled correlations ($r_{n,\text{shuffled}}$) were described using a zero-lag Pearson's correlation coefficient between the neural activity trace and the reverse of the pupil diameter trace, locomotion speed trace, or neural activity trace of one of the cells in a cell–cell pair. A cell was considered to be a positive responder to locomotion if $r_n > P_{95}(r_{N,\text{shuffled}})$ and a negative responder if $r_n < P_5(r_{N,\text{shuffled}})$, where $r_{N,\text{shuffled}}$ was the distribution of $r_{n,\text{shuffled}}$ values for WT mice.

Experimental design and statistical analyses. Statistical analysis and data visualization were performed using built-in MATLAB functions. Given the nested structure and non-normality of our data, we utilized generalized linear mixed effects modeling to determine the statistical significance of genotype differences, unless otherwise indicated in the text or figure legend. For each comparison, a generalized linear mixed effects model was constructed using the MATLAB function "fitglme" and the model formula:

$$\text{property} \sim \text{genotype} + (1|\text{mouse number}),$$

which specified a random intercept model in which genotype was considered a fixed effect and mouse number was considered a random effect. For the immunohistochemistry experiment (Fig. 5), cell type (PV vs Ndnf-IN) was specified as the fixed effect in place of genotype. A 95% confidence interval (CI) of the fixed effect coefficient of the model and a *p*-value (generated from the *F*-test for the null hypothesis that the fixed effect coefficient is equal to zero) are reported for each genotype comparison.

In accordance with the NIH guidelines, we included both male and female mice in roughly equal numbers in our study. To assess the possible contribution of sex as a biological variable, we compared the results of the above analysis for the genotype comparisons of intrinsic electrophysiologic property data into an additional analysis using the model formula:

$$\text{property} \sim \text{genotype} + \text{sex} + (1|\text{mouse\_number}).$$

We performed an *F*-test of the null hypothesis that the fixed effects coefficients for genotype and sex are equal to 0 and found no significant differences across all intrinsic electrophysiologic properties at both developmental timepoints.

Sample sizes were based on previous studies of genotype differences in electrophysiologic properties and in vivo functional imaging in mouse models of DS. Values for individual cells/mice are shown whenever possible, and the *n* values and errors reported in all line and bar graphs are indicated in the main text or figure legends.

Code and data accessibility. All analyses were performed using custom code implemented in MATLAB (MathWorks). All code is available through GitHub: https://github.com/GoldbergNeuroLab/Liebergall-Goldberg-2023. Source data files for all figures and tables have been made available at the Goldberg Lab G-Node: https://gin.g-node.org/GoldbergNeuroLab/Liebergall-Goldberg-2023.

Results

Intrinsic excitability of Ndnf-INs is preserved in *Scn1a*+/− mice during the acute and chronic phases of DS pathogenesis

Prior work in DS mouse models (*Scn1a*+/− mice) demonstrates impaired excitability of three of the major subclasses of neocortical INs—PV, SST, and VIP-INs—which manifests as a depolarized AP threshold, decreased maximal FF, and a decrease in the slope of the current–FF relationship (Tai et al., 2014; Favero et al., 2018; Goff and Goldberg, 2019) consistent with impaired Na^+ channel function. This persists in conditional mouse models in which *Scn1a* is selectively deleted in specific IN subclasses, indicating a cell-autonomous effect (Cheah et al., 2012; Tai et al., 2014; Rubinstein et al., 2015; Goff et al., 2023). Publicly available single-cell RNA sequencing data from the neocortex and the hippocampus suggest that Ndnf-INs express *Scn1a* transcripts at levels similar to other IN subclasses (Yao et al., 2021). Hence, we predicted that Ndnf-INs would also rely on Nav1.1 for AP generation and propagation such that heterozygous loss of *Scn1a* would result in impaired excitability of Ndnf-INs.

To test this hypothesis, we performed whole-cell current-clamp recordings of Ndnf-INs in the primary somatosensory cortex in acute brain slices from male and female *Scn1a*+/− mice and WT age-matched littermate controls (Fig. 1*A*). Recordings performed in mice aged P16–21 correspond with the acute phase of the disease during which *Scn1a*+/− mice experience the highest frequency of spontaneous seizures and highest rate of sudden unexpected death in epilepsy (SUDEP) (Yu et al., 2006; Mistry et al., 2014), and during which PV-INs show the greatest impairment in intrinsic excitability (Favero et al., 2018; Kaneko et al., 2022). We determined the passive membrane properties, properties of individual APs, and properties of the

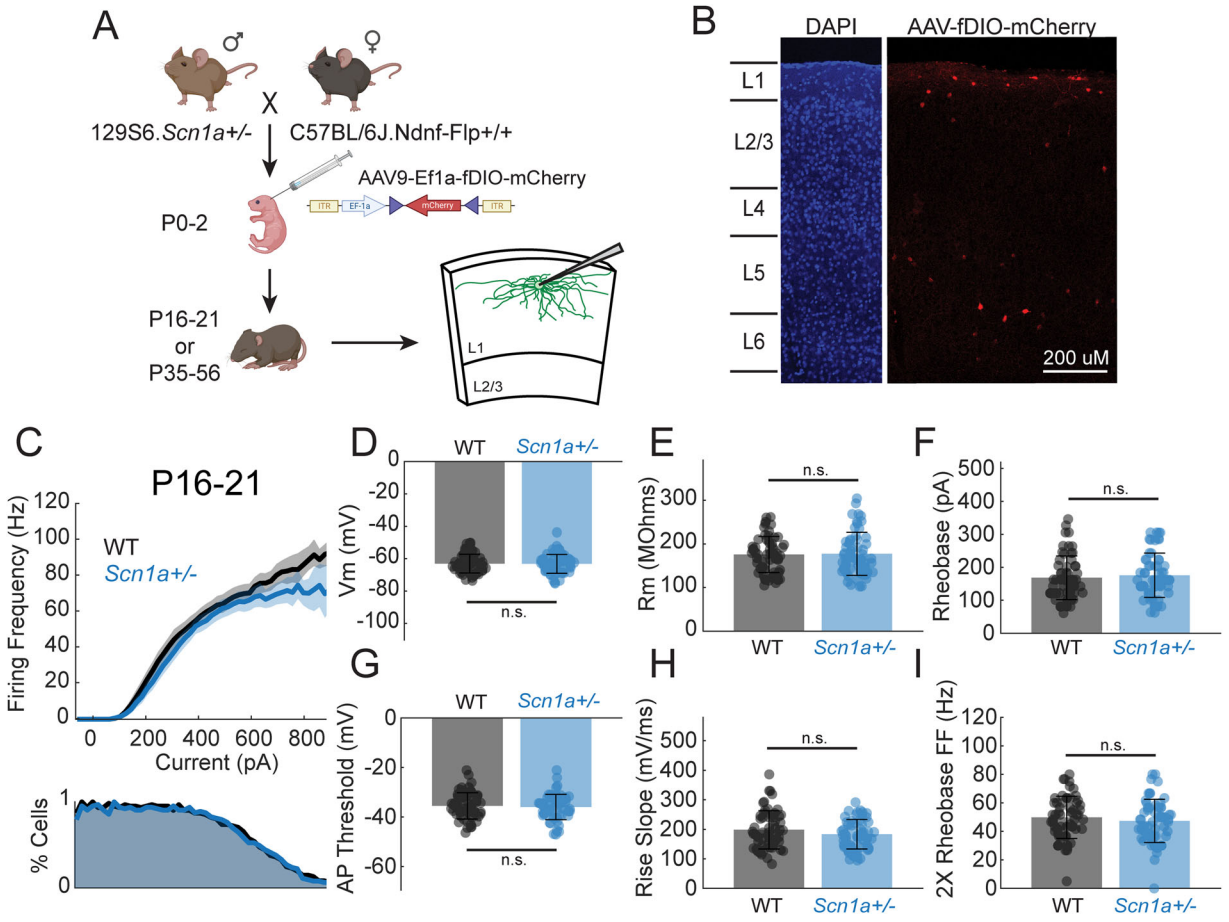

Figure 1. Intrinsic excitability of Ndnf-INs is preserved in *Scn1a*+/− mice during the acute phase of DS pathogenesis. ***A***, Schematic of the breeding strategy and AAV injections to fluorescently label Ndnf-INs in acute brain slices from *Scn1a*+/− mice and age-matched WT littermates. ***B***, Representative image of Flp-dependent mCherry expression predominantly restricted to Layer 1 of the neocortex. ***C***, Spike F–I curves (top) from whole-cell current-clamp recordings of Ndnf-INs in the primary somatosensory cortex in P16–21 ($n = 58$ cells from $N = 16$ WT mice; $n = 58$ cells from $N = 13$ *Scn1a*+/− mice). The shaded regions indicate the 95% bootstrap CIs. Recordings were included in the analysis up to the maximum steady-state FF of the cell. A cumulative distribution function (bottom) indicates the proportion of cells included in the analysis at each current injection. ***D–I***, Summary data for (***D***) resting membrane potential, (***E***) input resistance, (***F***) rheobase, (***G***) AP threshold, (***H***) maximum rise slope, and (***I***) FF at 2× rheobase current injection in all Ndnf-INs from P16–21 *Scn1a*+/− mice and age-matched WT littermate controls. Error bars indicate standard deviation. Summary data for other measured intrinsic properties are listed in Table 1. Ninety-five percent CIs for all comparisons are listed in Table 2.

Table 1. Summary statistics for intrinsic properties of Ndnf-INs by genotype and subpopulation at P16–21

Genotype	WT			*Scn1a*+/−		
Firing pattern	All	NGFC	Canopy	All	NGFC	Canopy
Group count	58	35	23	58	36	22
Age	18.71 ± 0.22	18.77 ± 0.27	18.61 ± 0.38	18.19 ± 0.14	18.19 ± 0.18	18.18 ± 0.21
Vm (mV)	−63.07 ± 0.76	−64.07 ± 0.91	−61.55 ± 1.29	−63.20 ± 0.77	−63.57 ± 0.96	−62.60 ± 1.29
Rm (mOhms)	175.61 ± 5.43	175.28 ± 7.33	176.11 ± 8.13	177.33 ± 6.48	180.87 ± 8.04	171.54 ± 11.03
Time constant	9.02 ± 0.25	8.53 ± 0.32	9.76 ± 0.38	9.19 ± 0.33	9.05 ± 0.40	9.41 ± 0.58
Rheobase (pA)	168.31 ± 8.69	163.28 ± 10.49	175.97 ± 15.17	175.88 ± 8.82	175.93 ± 11.69	175.78 ± 13.56
AP threshold (mV)	−35.51 ± 0.70	−33.96 ± 0.83	−37.87 ± 1.06	−35.95 ± 0.67	−34.45 ± 0.78	−38.41 ± 1.04
AP rise time (ms)	0.50 ± 0.01	0.51 ± 0.01	0.50 ± 0.02	0.54 ± 0.01	0.56 ± 0.02	0.51 ± 0.02
Max rise slope (mV/ms)	198.31 ± 8.50	195.99 ± 10.86	201.85 ± 13.9	183.25 ± 6.57	177.49 ± 7.95	192.68 ± 11.39
AP half-width (ms)	0.76 ± 0.02	0.78 ± 0.02	0.73 ± 0.03	0.82 ± 0.03	0.87 ± 0.04	0.74 ± 0.03
AP peak (mV)	17.99 ± 1.22	18.70 ± 1.53	16.92 ± 2.04	17.32 ± 1.1	17.86 ± 1.31	16.43 ± 1.96
AP amplitude (mV)	53.50 ± 1.35	52.66 ± 1.62	54.79 ± 2.37	53.27 ± 1.18	52.31 ± 1.25	54.84 ± 2.33
AHP amplitude (mV)	11.70 ± 0.69	14.17 ± 0.85	7.94 ± 0.61	10.79 ± 0.67	13.22 ± 0.73	6.82 ± 0.75
Sag (%)	0.65 ± 0.09	0.61 ± 0.12	0.71 ± 0.16	0.66 ± 0.10	0.71 ± 0.14	0.58 ± 0.15
APs at rheobase	3.38 ± 0.38	3.77 ± 0.48	2.78 ± 0.62	3.05 ± 0.28	3.25 ± 0.28	2.73 ± 0.58
Max IFF (Hz)	247.68 ± 5.89	248.24 ± 7.32	246.83 ± 10.05	256.52 ± 14.50	232.3 ± 6.61	296.16 ± 35.55
Max SSFF (Hz)	84.80 ± 2.25	88.10 ± 2.79	79.78 ± 3.60	76.55 ± 2.14	78.10 ± 2.51	74.02 ± 3.89
FF at 2× rheobase (Hz)	49.80 ± 1.94	46.81 ± 2.23	54.35 ± 3.38	47.36 ± 1.99	46.71 ± 2.38	48.41 ± 3.59
Latency to first spike (ms)	109.78 ± 18.52	161.35 ± 27.43	31.29 ± 2.63	122.41 ± 17.54	179.02 ± 23.68	29.76 ± 3.45

Mean and standard error of passive membrane properties, properties of individual APs, and properties of repetitive firing from current-clamp recordings of Layer 1 Ndnf-INs in the primary somatosensory cortex of P16–21 *Scn1a*+/− mice and age-matched WT littermate controls. Ninety-five percent CIs for all comparisons are listed in Table 2.

Table 2. Statistical analysis of intrinsic properties of Ndnf-INs by genotype and subpopulation at P16–21

Comparison	All WT vs *Scn1a*+/−	WT NGFC vs *Scn1a*+/− NGFC	WT Canopy vs *Scn1a*+/− Canopy	WT NGFC vs Canopy	*Scn1a*+/− NGFC vs Canopy
Vm (mV)	(−2.5, 3.4)	(−2.4, 4.3)	(−5.2, 3.6)	(−5.2,0.8)	(−4.5,0.8)
Rm (mOhms)	(−14.9, 18.3)	(−15.8, 27.0)	(−31.4, 22.3)	(−22.9, 21.2)	(−17.1, 35.7)
Time constant	(−0.6, 1.0)	(−0.5, 1.5)	(−2.0, 1.7)	(−2.2, −0.3)	(−1.7, 1.0)
Rheobase (pA)	(−16.7, 31.9)	(−18.3, 43.6)	(−40.4, 40)	(−47.7, 22.6)	(−35.9, 36.2)
AP threshold (mV)	(−2.3, 2.4)	(−2.3, 3.3)	(−4.4, 2.6)	(1.0, 6.2)*,†	(1.7, 6.6)*,†
AP rise time (ms)	(−0.01, 0.08)	(0.002, 0.11)*,†	(−0.04, 0.07)	(−0.03,0.03)	(−0.002, 0.09)
Max rise slope (mV/ms)	(−56.5, 15.6)	(−65.1, 10.8)	(−60.3, 32.8)	(−26.6, 23.4)	(−38.4, 11)
AP half-width (ms)	(−0.03, 0.16)	(−0.02, 0.21)†	(−0.1, 0.13)	(−0.02, 0.1)	(0.02, 0.23)*,†
AP peak (mV)	(−5.9, 5.2)	(−6.2, 5.2)	(−9.2, 6.1)	(−2.2, 4.7)	(−1.7, 6.3)
AP amplitude (mV)	(−6.1, 4.4)	(−6.6, 4.1)	(−6.6, 6.6)	(−6.6, 2.3)	(−7.3, 2.2)
AHP amplitude (mV)	(−2.9, 1.6)	(−3.1, 2.5)	(−3.9, 0.7)	(3.8, 8.2)*	(4.6, 8.8)*
Sag (%)	(−0.4, 0.5)	(−0.4, 0.6)	(−0.6, 0.6)	(−0.5, 0.3)	(−0.4, 0.3)
APs at rheobase	(−1.4, 0.7)	(−1.7, 0.7)	(−1.7, 1.6)	(−0.5, 2.5)	(−0.6, 1.7)
Max IFF (Hz)	(−23.3, 39.5)	(−47, 10.4)	(−22.6, 121.0)†	(−13.5, 29.0)	(−120.8, −7.0)*,†
Max SSFF (Hz)	(−16.5, 0.4)	(−18.3, −1.2)*	(−16.9, 10.3)	(1.5, 18.6)*	(−4.5, 11.1)
FF at 2× rheobase (Hz)	(−10.6, 5.3)	(−9.2, 7.9)	(−17.9, 4.9)	(−13, 1.6)	(−8.4, 5.6)
Latency to first spike (ms)	(−37.5, 62.7)	(−53.5, 88.8)	(−10.8, 7.3)	(63.1, 197.0)*,†	(89.2, 209.3)*,†

Ninety-five percent CIs for genotype and subpopulation comparisons of the intrinsic properties of Layer 1 Ndnf-INs from P16–21 *Scn1a*+/− mice and WT littermate controls listed in Table 1.
*Indicates that genotypes are statistically different (p-value <0.05).
†Indicates that genotypes are not statistically equivalent (95% CI includes an upper or lower limit of effect size).

repetitive firing of WT and *Scn1a*+/− Layer 1 Ndnf-INs (Table 1). Surprisingly, these recordings did not reveal any significant differences between Ndnf-INs from *Scn1a*+/− mice and WT littermate controls (Tables 1, 2, Fig. 1).

Previous studies have demonstrated that Ndnf comprises at least two distinct subpopulations of neurons in Layer 1 of the neocortex (Schuman et al., 2019). Because these populations have different electrophysiologic properties, it is possible that they express unique sets of voltage-gated ion channels and thus could show differential expression of/reliance on Nav1.1. To account for this possibility, we reanalyzed the data after dividing Ndnf-INs into two subpopulations—NGFCs and Canopy cells—based on the defining properties as previously reported (Schuman et al., 2019; Fig. 2*A–F*). There were roughly equal proportions of NGFCs and Canopy cells in both genotypes (Fig. 2*G*), as well as differences in AP threshold, AHP amplitude, and the latency to the first spike at a rheobase current injection between subpopulations (Tables 1, 2, Fig. 2*M*). However, there were no differences between the intrinsic properties of either NGFCs or Canopy cells in *Scn1a*+/− mice when compared with WT controls, other than a small but statistically significant increase in the rise time of the first AP in repetitive trains of tonic spiking and a small decrease in the maximum steady-state FF that was observed in NGFCs only (Tables 1, 2, Fig. 2).

IN dysfunction in DS is developmentally regulated in a subclass-specific pattern. Dysfunctional PV-INs appear to recover excitability as the mouse transitions to young adulthood, whereas the intrinsic excitability of VIP-INs remains impaired into adulthood (Favero et al., 2018; Goff and Goldberg, 2019). To identify a potential developmental window of Ndnf-IN dysfunction, we repeated recordings of Ndnf-INs in mice aged P35–56, which corresponds to the chronic phase of the disease during which mice display a decreased frequency of spontaneous seizures and SUDEP, but still show the chronic ASD-like behavioral phenotypes of DS (Yu et al., 2006; Han et al., 2012). Recordings at this later timepoint also did not reveal any obvious deficits in *Scn1a*+/− Ndnf-IN intrinsic excitability relative to WT (Tables 3, 4, Fig. 3). In a subgroup analysis of P35–56 NGFCs and Canopy cells, there was a small difference in max rise slope in NGFCs in addition to small differences in AP peak and amplitude (Tables 3, 4, Fig. 4), possibility reflecting a subtle decrease in Na^+ current density in NGFCs from *Scn1a*+/− mice. In summary, Ndnf-INs are the only IN subclass so far examined in mouse models of DS that do not show prominent impairment of intrinsic excitability across development as measured by whole-cell current-clamp recordings.

Absence of Nav1.1 at the Ndnf-IN AIS

Given that *Scn1a*+/− Ndnf-INs do not show any changes in Na^+ channel-dependent intrinsic properties in whole-cell patch-clamp recordings, we hypothesized that Ndnf-INs do not express Nav1.1 or have a significantly lower density of Nav1.1 channels relative to other IN subclasses. To assess this hypothesis, we performed immunohistochemical staining for Nav1.1 protein, along with the AIS marker Ankyrin-G, in WT.Ndnf-Flp mice injected with an AAV encoding a Flp-dependent mCherry protein (Fig. 5). No Layer 1 primary somatosensory cortex Ndnf-INs demonstrated strong Nav1.1 immunoreactivity at any point along the AIS (as defined by Ankyrin-G staining; Fig. 5*A*,*B*,*E*). As a positive control, in parallel, we also performed immunostaining for Nav1.1 and Ankyrin-G in WT.PV-Cre.tdTomato mice. In line with previous work (Ogiwara et al., 2007; Duflocq et al., 2008; Lorincz and Nusser, 2008), we demonstrated strong Nav1.1 immunoreactivity at the proximal AIS of Layer 2/3 primary somatosensory cortex PV-INs (Fig. 5*C–E*). This finding suggests that the lack of impairment in intrinsic excitability in Ndnf-INs relative to PV-INs in *Scn1a*+/− mice is due to the absence of Nav1.1 expression at the AIS in Ndnf-INs and a lack of reliance of Ndnf-INs on Nav1.1 for spike generation relative to other IN subtypes.

Normal Na^+ current density in Ndnf-INs in *Scn1a*+/− mice

Although Ndnf-INs do not express detectable Nav1.1 protein at the AIS, it is difficult to establish with certainty that Ndnf-INs do not express any Nav1.1 whatsoever. Ion channels constitute a small proportion of total membrane protein, and immunohistochemical staining may not easily distinguish between proteins retained in the endoplasmic reticulum and those that are successfully trafficked to the membrane (Kole et al., 2008; Hu et al., 2009;

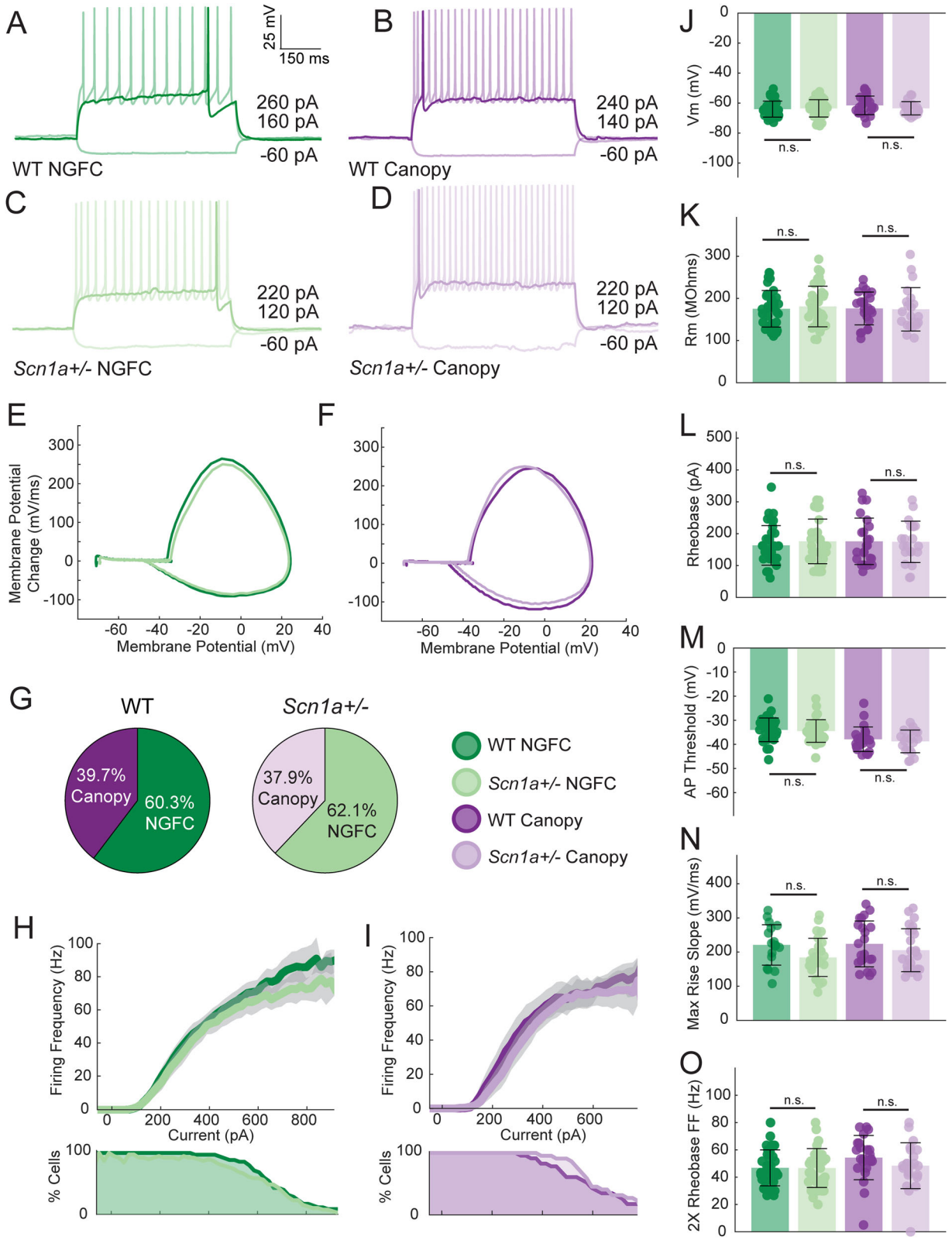

Figure 2. Intrinsic excitability of NGFCs and Canopy cells is preserved in *Scn1a*+/− mice during the acute phase of DS pathogenesis. ***A–D***, Representative traces from whole-cell current-clamp recordings of (***A***, ***C***) NGFCs and (***B***, ***D***) Canopy cells from the primary somatosensory cortex of P16–21 WT and *Scn1a*+/− mice in response to −60 pA, rheobase, and 100 pA over rheobase 600 ms square-wave current injections. ***E***, ***F***, Representative phase plots of APs in (***E***) NGFCs and (***F***) Canopy cells from P16–21 WT and *Scn1a*+/− mice. ***G***, Relative proportions of Ndnf-IN classified as NGFCs versus Canopy cells in P16–21 WT and *Scn1a*+/− mice. ***H***, ***I***, F–I curves from whole-cell current-clamp recordings of (***H***) NGFCs ($n = 35$ cells from $N = 15$ WT mice, 36 cells from $N = 12$ *Scn1a*+/− mice) and (***I***) Canopy cells ($n = 23$ cells from $N = 11$ WT mice; $n = 22$ cells from $N = 9$ *Scn1a*+/− mice) from P16–21 WT and *Scn1a*+/− mice. The shaded regions indicate the 95% bootstrap CIs. Recordings were included in the analysis up to the maximum steady-state FF of the cell. Cumulative distribution functions (bottom) indicate the proportion of cells included in the analysis at each current injection. ***J–O***, Summary data for (***J***) resting membrane potential, (***K***) input resistance, (***L***) rheobase, (***M***) AP threshold, (***N***) maximum rise slope, and (***O***) FF at 2× the rheobase current injection in NGFCs and Canopy cells from P16–21 *Scn1a*+/− mice and age-matched WT littermate controls. Error bars indicate standard deviation. Summary data for other measured intrinsic properties are listed in Table 1. Ninety-five percent CIs for all comparisons are listed in Table 2.

Table 3. Summary statistics for intrinsic properties of Ndnf-INs by genotype and subpopulation at P35–56

Genotype	WT			*Scn1a*+/−		
Firing pattern	All	NGFC	Canopy	All	NGFC	Canopy
Group count	39	17	22	52	27	25
Age	44.59 ± 1.30	46.82 ± 2.13	42.86 ± 1.56	42.23 ± 1.07	43.59 ± 1.52	40.76 ± 1.48
Vm (mV)	−67.86 ± 0.91	−71.09 ± 1.16	−65.36 ± 1.10	−68.12 ± 0.89	−69.91 ± 1.16	−66.19 ± 1.27
Rm (mOhms)	168.47 ± 7.33	161.16 ± 13.24	174.12 ± 8.1	189.46 ± 8.43	182.35 ± 11.31	197.14 ± 12.64
Time constant	7.65 ± 0.29	7.09 ± 0.48	8.09 ± 0.35	8.17 ± 0.25	7.87 ± 0.37	8.51 ± 0.34
Rheobase (pA)	155.40 ± 9.42	162.21 ± 17.3	150.15 ± 10.27	144.75 ± 8.07	137.78 ± 10.12	152.27 ± 12.78
AP threshold (mV)	−36.77 ± 0.83	−34.13 ± 1.23	−38.81 ± 0.92	−34.87 ± 0.76	−33.01 ± 1.22	−36.87 ± 0.71
AP rise time (ms)	0.48 ± 0.01	0.48 ± 0.02	0.47 ± 0.02	0.49 ± 0.01	0.50 ± 0.02	0.48 ± 0.02
Max rise slope (mV/ms)	223.17 ± 10.19	222.33 ± 14.70	223.82 ± 14.35	194.44 ± 8.29	184.27 ± 10.75	205.41 ± 12.6
AP half-width (ms)	0.74 ± 0.02	0.74 ± 0.03	0.74 ± 0.03	0.77 ± 0.02	0.83 ± 0.04	0.71 ± 0.02
AP peak (mV)	19.47 ± 1.52	22.18 ± 2.09	17.37 ± 2.09	16.61 ± 1.19	16.62 ± 1.36	16.61 ± 2.02
AP amplitude (mV)	56.24 ± 1.43	56.31 ± 2.22	56.18 ± 1.92	51.48 ± 1.44	49.63 ± 1.79	53.49 ± 2.25
AHP amplitude (mV)	9.78 ± 1.03	13.66 ± 1.44	6.79 ± 1.08	12.88 ± 0.86	16.51 ± 0.93	8.96 ± 1.03
Sag (%)	1.14 ± 0.12	0.80 ± 0.11	1.41 ± 0.18	1.16 ± 0.11	0.97 ± 0.11	1.37 ± 0.19
APs at rheobase	2.74 ± 0.42	3.65 ± 0.71	2.05 ± 0.45	2.58 ± 0.25	3.19 ± 0.32	1.92 ± 0.34
Max IFF (Hz)	229.43 ± 10.99	229.16 ± 15.13	229.63 ± 15.90	233.02 ± 8.51	221.24 ± 10.25	245.74 ± 13.58
Max SSFF (Hz)	70.26 ± 4.12	75.98 ± 4.33	65.83 ± 6.42	68.01 ± 2.92	70.68 ± 3.00	65.13 ± 5.14
FF at 2× rheobase (Hz)	44.27 ± 2.33	43.14 ± 1.99	45.15 ± 3.88	41.63 ± 1.84	39.69 ± 2.02	43.73 ± 3.15
Latency to first spike (ms)	86.95 ± 17.95	167.58 ± 32.05	24.65 ± 2.31	127.62 ± 21.78	222.53 ± 32.59	25.13 ± 3.27

Mean and standard error of passive membrane properties, properties of individual APs, and properties of repetitive firing from current-clamp recordings of Layer 1 Ndnf-INs in the primary somatosensory cortex of P35–56 *Scn1a*+/− mice and age-matched WT littermate controls. Ninety-five percent CIs for all comparisons are listed in Table 4.

Table 4. Statistical analysis of intrinsic properties of Ndnf-INs by genotype and subpopulation at P35–56

Comparison	All WT vs *Scn1a*+/−	WT NGFC vs *Scn1a*+/− NGFC	WT Canopy vs *Scn1a*+/− Canopy	WT NGFC vs Canopy	*Scn1a*+/− NGFC vs Canopy
Vm (mV)	(−4.0, 3.1)	(−2.4, 4.7)	(−4.8, 3.3)	(−7.2, −2.3)*	(−6.7, −0.2)*
Rm (mOhms)	(−2.5, 50.0)	(−24.5, 72.3)	(−7.5, 53.5)	(−42.2, 16.3)	(−50.2, 14.5)
Time constant	(−0.4, 1.5)	(−0.8, 2.5)	(−0.6, 1.4)	(−2.1, 0.1)	(−1.7, 0.2)
Rheobase (pA)	(−51.5, 13.3)	(−75.2, 16.5)	(−31.2, 35.2)	(−26.7, 38.7)	(−46.6, 16.5)
AP threshold (mV)	(−1.7, 4.3)	(−4.5, 4.8)	(−0.3, 4.2)	(1.9, 7.3)*,†	(1.5, 6.7)*,†
AP rise time (ms)	(−0.03, 0.08)	(−0.04, 0.11)†	(−0.07, 0.08)	(−0.05, 0.04)	(−0.03, 0.08)
Max rise slope (mV/ms)	(−73.1, 2.4)	(−81.3, −1.6)*	(−63.3, 37.3)	(−20.7, 44.3)	(−58.9, −1.4)*
AP half-width (ms)	(−0.05, 0.16)	(−0.03, 0.26)†	(−0.13, 0.06)	(−0.08, 0.07)	(0.06, 0.2)*
AP peak (mV)	(−9.1, 1.7)	(−11.3, −0.7)*,†	(−6.9, 7.7)	(1.5, 10.9)*,†	(−5.8, 2.7)
AP amplitude (mV)	(−10.0, 0.5)	(−12.3, −1.0)*,†	(−8.8, 5.7)	(−4.1, 6.4)	(−10.6, 0.03)†
AHP amplitude (mV)	(−0.6, 5.9)	(−2.0, 5.9)	(−1.4, 5.4)	(3.9, 10.3)*,†	(5.1, 10.1)*,†
Sag (%)	(−0.4, 0.4)	(−0.2, 0.5)	(−0.6, 0.5)	(−1.0, −0.1)*,†	(−0.8, 0.02)
APs at rheobase	(−1.1, 0.7)	(−1.8, 0.9)	(−1.3, 1.1)	(0.01, 3.2)*	(0.6, 2.3)*
Max IFF (Hz)	(−41.2, 50.5)	(−52.1, 39.4)	(−47.1, 70.1)	(−31.9, 35.5)	(−35.1, 16.9)
Max SSFF (Hz)	(−15.4, 11.2)	(−15.4, 4.8)	(−18.6, 17)	(−6.7, 21.2)	(−6.0, 17.1)
FF at 2× rheobase (Hz)	(−10.2, 3.9)	(−12.4, 3.7)	(−11.6, 8.8)	(−12.1, 6.3)	(−10.9, 3.0)
Latency to first spike (ms)	(−18.4, 101.4)†	(−46.5, 155.6)†	(−7.6, 8.6)	(87.3, 198.5)*,†	(130.4, 264.4]*,†

Ninety-five percent CIs for genotype and subpopulation comparisons of the intrinsic properties of Layer 1 Ndnf-INs from P16–21 *Scn1a*+/− mice and WT littermate controls are listed in Table 3.
*Indicates that genotypes are statistically different (*p*-value <0.05).
†Indicates that genotypes are not statistically equivalent (95% CI includes an upper or lower limit of effect size).

Lorincz and Nusser, 2010). To assess whether loss of *Scn1a* in Ndnf-INs might manifest as reduced somatic Na^+ current density, we performed voltage-clamp recordings of Na^+ currents in nucleated outside-out macropatches from Ndnf-INs in brain slices of P16–21 *Scn1a*+/− mice and WT littermate controls (Fig. 6*A–D*). This technique facilitates high signal-to-noise recording of Na^+ currents under favorable space clamp conditions from confirmed genetically defined cell types in acute brain slices (Tamagnini, 2021). There were no genotype differences in the voltage dependence of activation of the recorded Na^+ currents, as might be expected due to the heterozygous loss of Nav1.1 (Fig. 6*G*). However, we also found no difference in the peak Na^+ current density in *Scn1a*+/− Ndnf-INs relative to WT controls [Fig. 6*E,F*; WT, −153.5 pA/pF; *Scn1a*+/−, −134.4 pA/pF; 95% CI = (−30.6, 68.9); *p*-value = 0.44]. These data indicate that either (1) Nav1.1 minimally contributes to somatic Na^+ current in WT Ndnf-INs or (2) *Scn1a*+/− Ndnf-IN Na^+ current has normalized via compensation, perhaps via upregulation of non-Nav1.1 Nav1.X paralog(s).

Synaptic transmission between Ndnf-INs remains intact in *Scn1a*+/− mice

Nav1.1 channels are preferentially trafficked to axon branch points and nodes of Ranvier, in addition to the proximal AIS (Duflocq et al., 2008; Kaneko et al., 2022). Thus, we considered the possibility that AP propagation along the axon and synaptic transmission could be affected, while the somatic AP (as measured by whole-cell patch-clamp and nucleated macropatch

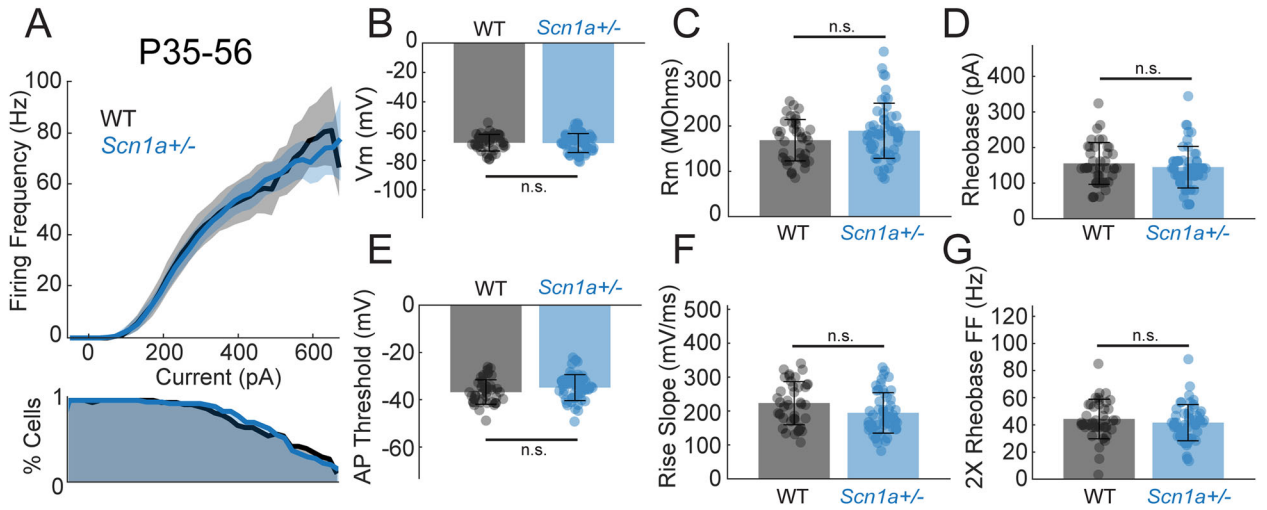

Figure 3. Intrinsic excitability of Ndnf-INs is preserved in *Scn1a*+/− mice during the chronic phase of DS pathogenesis. ***A***, Spike F–I curves (*top*) from whole-cell current-clamp recordings of Ndnf-INs in the primary somatosensory cortex of P35–56 mice ($n = 39$ cells from $N = 10$ WT mice; $n = 52$ cells from $N = 11$ *Scn1a*+/− mice). The shaded regions indicate the 95% bootstrap CIs. Recordings were included in the analysis up to the maximum steady-state FF of the cell. A cumulative distribution function (*bottom*) indicates the proportion of cells included in the analysis at each current injection. ***B–G***, Summary data for (***B***) resting membrane potential, (***C***) input resistance, (***D***) rheobase, (***E***) AP threshold, (***F***) maximum rise slope, and (***G***) FF at 2× rheobase current injection in all Ndnf-INs from P35–56 *Scn1a*+/− mice and age-matched WT littermate controls. Error bars indicate standard deviation. Summary data for other measured intrinsic properties are listed in Table 3. Ninety-five percent CIs for all comparisons are listed in Table 4.

recordings) is relatively spared. In support of this possibility, studies of synaptic transmission by PV-INs in *Scn1a*+/− mice demonstrated an age-dependent dissociation between impairment of somatic spike generation and impairment of AP spike propagation/synaptic transmission (Kaneko et al., 2022). To assess whether synaptic connectivity or transmission is impaired in *Scn1a*+/− Ndnf-INs, we recorded unitary IPSCs between pairs of Layer 1 Ndnf-INs in P16–21 *Scn1a*+/− mice and WT littermate controls (Fig. 7*A*,*C*–*F*). There were no obvious differences in the connection probability between combinations of NGFC and Canopy Ndnf-INs in WT and *Scn1a*+/− mice (Fig. 7*B*). Similarly, there was no change in the amplitude [14.4 ± 2.3 vs 17.5 ± 2.4, 95% CI = (−3.4, 9.7), p-value = 0.34] or time to peak [6.8 ± 0.7 vs 6.1 ± 0.6, 95% CI = (−2.4, 1.1), p-value = 0.47] of the unitary IPSCs between connected pairs of Ndnf-INs in WT and *Scn1a*+/− mice (Fig. 7*G*,*H*). This lack of a genotype difference in the amplitude [NGFC 15.1 ± 3.0 vs 19.5 ± 3.3%, 95% CI = (−4.3, 13.2), p-value = 0.31; Canopy 12.5 ± 2.7 vs 12.7 ± 3.2, 95% CI = (−8.5, 8.9), p-value = 0.96] or time to peak [NGFC 7.7 ± 0.9 vs 6.0 ± 0.5, 95% CI = (−3.9, 0.3), p-value = 0.10; Canopy 4.1 ± 0.4 vs 6.2 ± 1.4, 95% CI = (−1.1, 8.9), p-value = 0.12] of unitary IPSCs held true when connections were grouped based on the subpopulation identity of the presynaptic cell (Fig. 7*I*,*J*). Of note, a substantial proportion of P16–21 Ndnf-IN pairs were also connected through gap junctions (27% of WT and 29% of *Scn1a*+/− chemically connected pairs; Fig. 7*K*,*L*). Nevertheless, we did not observe any genotype difference in the coupling coefficients of the electrical connections of Ndnf-IN pairs recorded in WT and *Scn1a*+/− Ndnf-INs (Fig. 7*M*; 2.1% vs 2.5%, p-value = 0.30).

Given that NGFCs have been shown to form synapses onto Layer 2/3 pyramidal neurons (Schuman et al., 2019), we additionally performed paired recordings of Ndnf-IN to Layer 2/3 pyramidal cell connections in P16–21 *Scn1a*+/− mice and age-matched littermate WT controls (Fig. 8). We similarly found no difference in the amplitude [WT 10.73 ± 2.0 vs *Scn1a*+/− 13.49 ± 2.7%, 95% CI = (−4.69, 1.94), p-value = 0.39] or time to peak [WT 8.52 ± 1.0 vs *Scn1a*+/− 8.96 ± 0.8%, 95% CI = (−2.10, 1.30), p-value = 0.63] of Ndnf-IN to Layer 2/3 pyramidal cell connections (Fig. 8*D*,*E*).

In vivo recruitment of Ndnf-INs during arousal is unchanged in *Scn1a*+/− mice relative to WT controls

Our ex vivo studies of Ndnf-IN function did not reveal any changes in intrinsic excitability of or synaptic transmission by *Scn1a*+/− Ndnf-INs, likely because WT Ndnf-INs do not rely on Nav1.1-containing Na^+ channels for spike generation or propagation. To investigate Ndnf-IN function in intact cortical circuits, we recorded the activity of Ndnf-INs in the primary somatosensory cortex of awake, behaving male and female *Scn1a*+/− mice and age-matched WT littermate controls using in vivo 2P calcium imaging. Previous work investigating the in vivo function of Ndnf-INs has shown these cells to be strongly recruited during arousal, likely due to activation of both nicotinic and muscarinic acetylcholine receptors during periods of high cholinergic tone (Brombas et al., 2014; Abs et al., 2018; Poorthuis et al., 2018; Cohen-Kashi Malina et al., 2021). Thus, we simultaneously recorded locomotion speed and pupil diameter to correlate Ndnf-IN activity with arousal (Fig. 9*A*).

Our recordings in WT mice aligned with the reported findings that Ndnf-IN activity is highly synchronous and is strongly recruited during periods of high arousal as measured by pupil diameter and locomotion speed (Fig. 9*B*–*G*). There were no genotype differences in the correlation of *Scn1a*+/− Ndnf-IN activity with locomotion speed (Fig. 9*B*), in the amplitude of the fluorescence transients at the onset of locomotion bouts (Fig. 9*H*), or in the proportion of Ndnf-INs recruited at the onset of locomotion bouts (Fig. 9*I*,*J*). Of note, the average locomotion speed and the number of locomotion bouts were not different between genotypes (Tran et al., 2020; Goff et al., 2023). Similarly, Ndnf-IN activity was correlated with pupil diameter in *Scn1a*+/− mice to the same degree as in WT controls (Fig. 9*C*). There were also no differences in measures

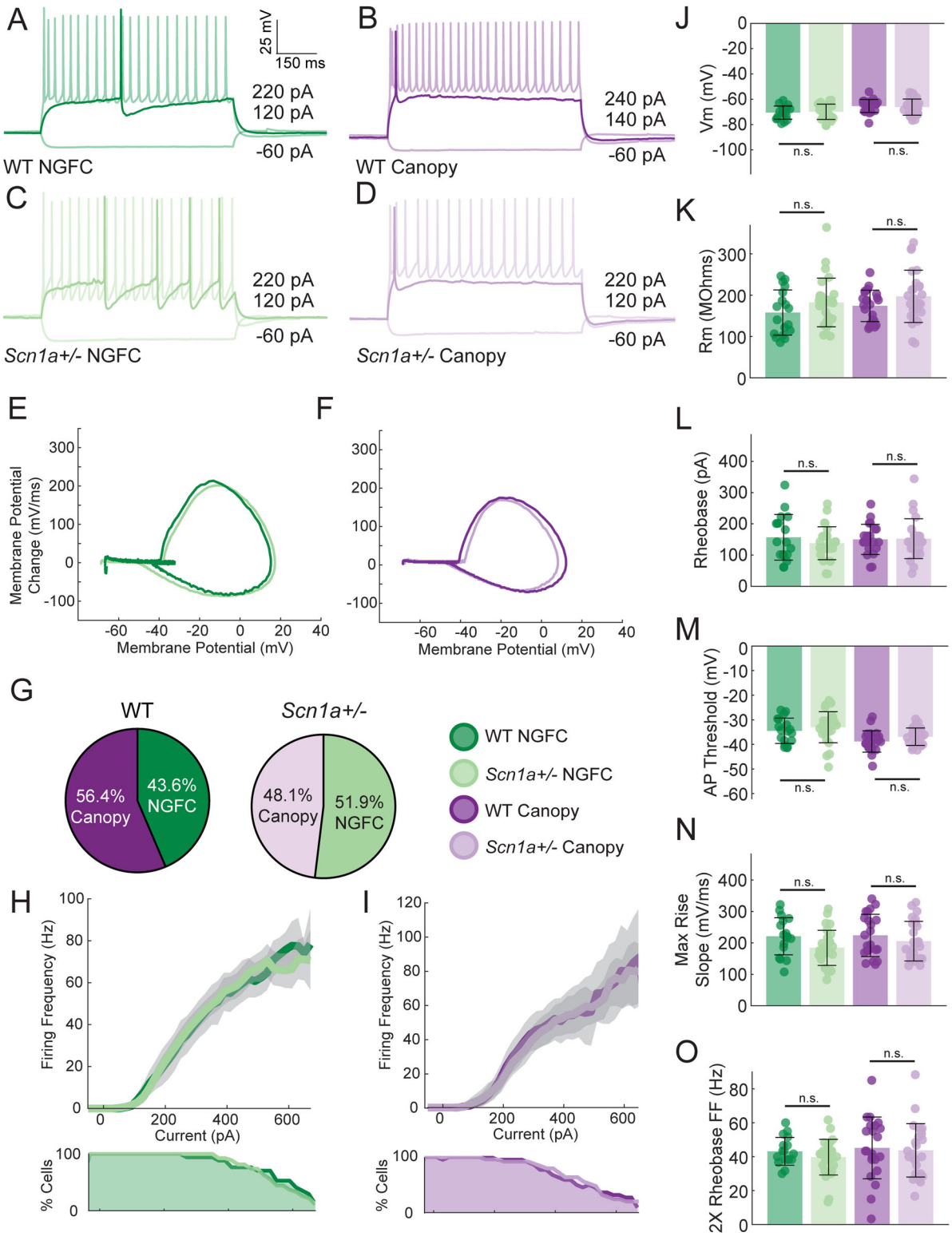

Figure 4. Intrinsic excitability of specific Ndnf-IN subclasses is preserved in *Scn1a*+/− mice during the chronic phase of DS pathogenesis. ***A–D***, Representative traces from whole-cell current-clamp recordings of (***A***, ***C***) NGFCs and (***B***, ***D***) Canopy cells from the primary somatosensory cortex of P35–56 WT and *Scn1a*+/− mice in response to −60 pA, rheobase, and 100 pA over rheobase 600 ms square-wave current injections. ***E***, ***F***, Representative phase plots of APs in (***E***) NGFCs and (***F***) Canopy cells from P16–21 WT and *Scn1a*+/− mice. ***G***, Relative proportions of Ndnf-IN classified as NGFCs versus Canopy cells in P35–56 WT and *Scn1a*+/− mice. ***H***, ***I***, F–I curves from whole-cell current-clamp recordings of (***G***) NGFCs ($n = 17$ cells from $N = 8$ WT mice; $n = 27$ cells from $N = 9$ *Scn1a*+/− mice) and (***H***) Canopy cells ($n = 22$ from $N = 9$ WT mice; $n = 25$ cells from $N = 8$ *Scn1a*+/− mice) from P35–56 WT and *Scn1a*+/− mice. The shaded regions indicate the 95% bootstrap CIs. Recordings were included in the analysis up to the maximum steady-state FF of the cell. Cumulative distribution functions (bottom) indicate the proportion of cells included in the analysis at each current injection. ***J–O***, Summary data for (***J***) resting membrane potential, (***K***) input resistance, (***L***) rheobase, (***M***) AP threshold, (***N***) maximum rise slope, and (***O***) FF at 2× the rheobase current injection in NGFCs and Canopy cells from P35–56 *Scn1a*+/− mice and age-matched WT littermate controls. Error bars indicate standard deviation. Summary data for other measured intrinsic properties are listed in Table 3. Ninety-five percent CIs for all comparisons are listed in Table 4.

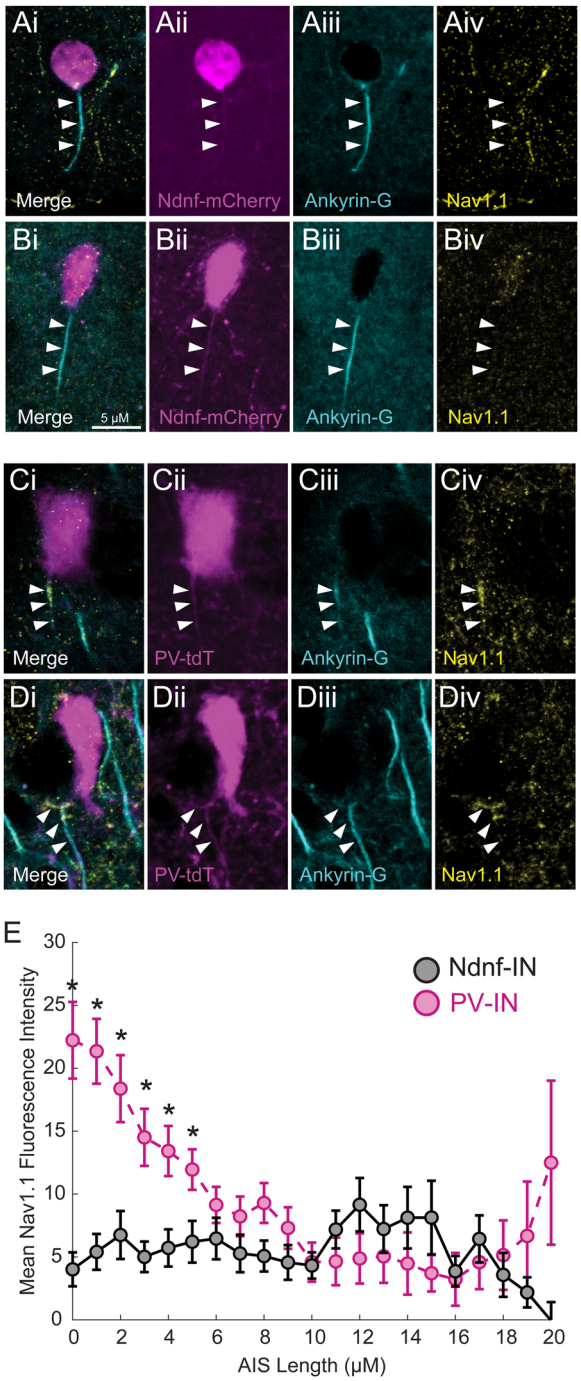

Figure 5. Absence of Nav1.1 protein at the AIS of neocortical Ndnf-INs. ***A–D***, Representative images of antibody staining for Ankyrin-G (cyan) and Nav1.1 (yellow) protein in (***A***, ***B***) Ndnf-INs or (***C***, ***D***) PV-INs in the primary somatosensory cortex of WT mice. Note that the proximal region of the AIS in PV-INs, but not Ndnf-INs, stains positive for Nav1.1. Images are average intensity projections of *z*-stack confocal images. ***E***, Quantification of background-subtracted mean fluorescence intensity as a function of distance along the AIS in WT Ndnf-INs (black, solid; $n = 41$ cells from 3 slices in each of 3 mice) and WT PV-INs (magenta, dashed; $n = 44$ cells from 3 to 5 slices in each of 3 mice). * indicates p-value <0.05 using a generalized linear mixed effects model where cell subclass is considered a fixed variable and mouse number is considered a random variable. Error bars indicate standard error of the mean.

of cell–cell synchrony between WT and *Scn1a*+/− Ndnf-INs (Fig. 9*D*). In summary, even in intact cortical circuits in vivo in awake, behaving mice, *Scn1a*+/− Ndnf-INs are efficiently recruited at the transition from quiet wakefulness to arousal and locomotion and show similar cell–cell synchrony to WT Ndnf-INs.

Discussion

Preserved Ndnf-IN function in *Scn1a*+/− mice: implications for the mechanism of DS

The prevailing hypothesis of DS pathophysiology posits that epilepsy and nonepilepsy endophenotypes are due to selective impairments in the excitability of cerebral cortex GABAergic INs (Catterall, 2018). Here, we show that neocortical Layer 1 Ndnf-INs are the only known major IN subclass that exhibits near-normal excitability and cortical microcircuit function across development in a mouse model of DS, as measured by patch-clamp recordings of intrinsic electrophysiologic properties, paired recordings of Ndnf-IN–mediated unitary postsynaptic currents, and in vivo recordings of Ndnf-IN recruitment during arousal. Our findings indicate that GABAergic INs display subclass-specific reliance on Nav1.1 for AP generation; thus, haploinsufficiency of *Scn1a* differentially affects discrete IN subclasses. This study emphasizes that subclass-specific heterogeneity of ion channel expression shapes the function of different cell types in the setting of pathology, which is highly relevant to refining our understanding of the mechanisms of neurologic disease and the development of therapeutic interventions.

Molecular determinants of Ndnf-IN excitability

Layer 1 of the neocortex is known to regulate top-down informational processing. However, a lack of subclass-specific genetic markers has made it challenging to systemically assess and manipulate the resident IN population of Layer 1. The recent discovery of Ndnf as a specific marker of the majority of Layer 1 INs has led to new insight into the electrophysiologic properties, anatomy, connectivity, and in vivo circuit function of this population of INs (Abs et al., 2018; Schuman et al., 2019; Anastasiades et al., 2021; Cohen-Kashi Malina et al., 2021). Knowledge of the molecular determinants of Ndnf-IN excitability is important to both understand the unique electrophysiologic properties of these cells and to specifically target Ndnf-INs for potential therapeutic intervention. Chittajallu et al. (2020) have recently described a subthreshold 4-AP–sensitive K^+ current reminiscent of an A-type conductance in NGFCs that is primarily composed of Kv4-containing channels and contributes to the late-spiking behavior of these cells. On the other hand, in a series of modeling studies, Meng et al. (2023) postulate that a slowly inactivating K^+ (SIK) channel contributes to the firing of Canopy cells, whereas the late-spiking and spike-frequency acceleration of NGFCs is best explained by a smaller SIK conductance. Less is known about the population of voltage-gated Na^+ channels expressed in Ndnf-INs. In single-cell RNA-sequencing experiments, Ndnf-INs express *Scn1a* transcripts at similar levels and in similar proportion to overall *ScnXa* transcript levels when compared with PV-INs, SST-INs, and VIP-INs in published single-cell RNA-seq datasets (Yao et al., 2021). Transcriptomic data, however, may not accurately reflect the density of Na^+ channel α subunit protein at the cell membrane due to the overall low level of ion channel transcripts present; the widespread posttranscriptional regulation of voltage-gated Na^+ channel α subunits through phosphorylation, ubiquitination, and arginine methylation (Onwuli and Beltran-Alvarez, 2016); and the necessary coexpression of Na^+ channel binding partners that facilitate

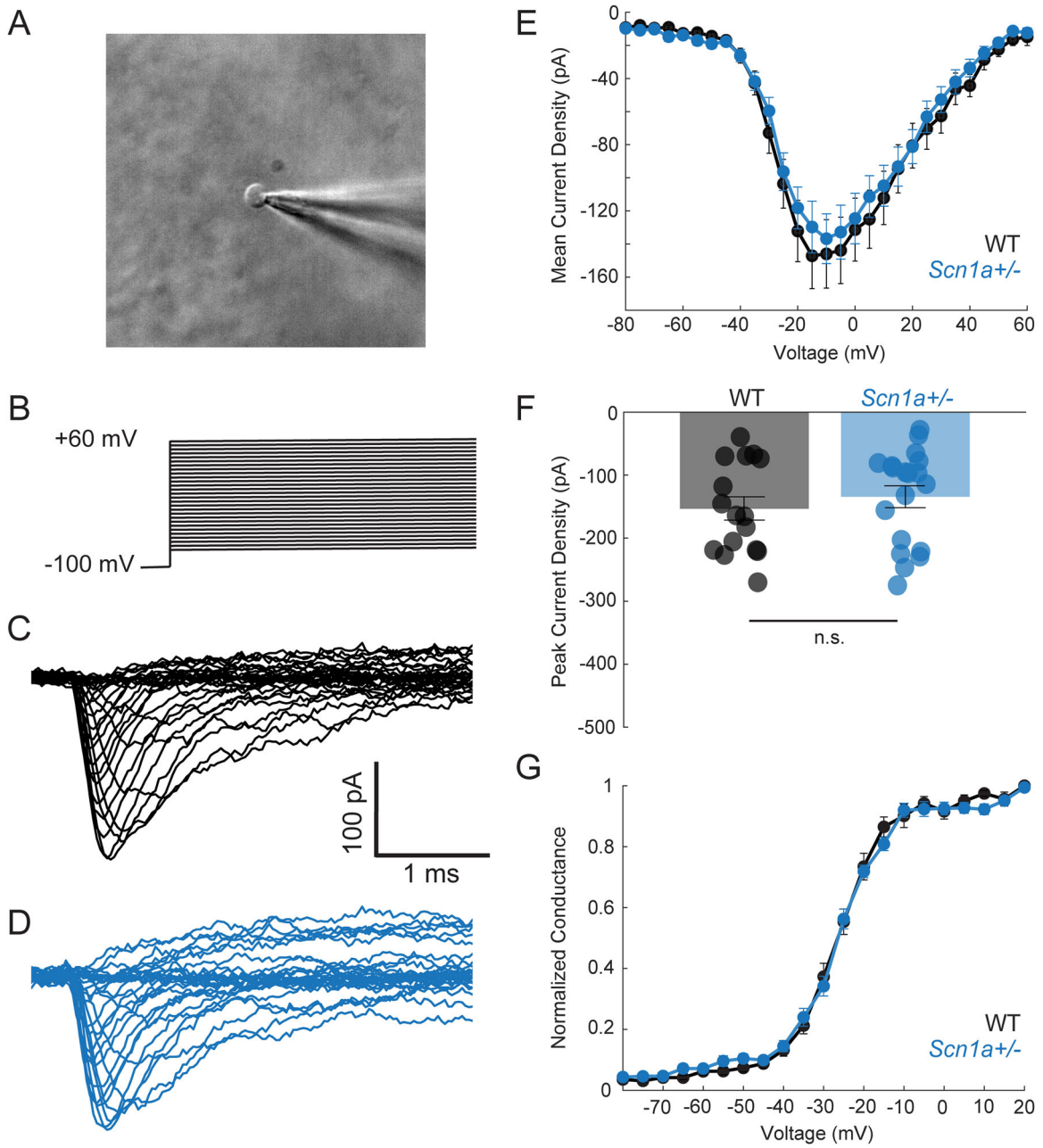

Figure 6. Ndnf-INs show normal Na^+ current density in *Scn1a*+/− mice relative to WT littermate controls. ***A***, IR-DIC image of a nucleated outside-out macropatch isolated from the soma of an Ndnf-IN in the primary somatosensory cortex. ***B***, Schematic of the protocol used to measure the voltage dependence of activation of Na^+ currents. Cells were stepped from a holding potential of 100 mV to between −80 and +60 mV in 5 mV increments. Note the presence of a small amount of residual outward K^+ current resistant to 10 mM TEA and 5 mM 4-AP. ***C***, ***D***, Representative voltage-clamp recordings of Na^+ currents in nucleated outside-out macropatches from Ndnf-INs in the primary somatosensory cortex of P16–21 (***C***) WT and (***D***) *Scn1a*+/− mice. ***E***, Mean peak current normalized to macropatch capacitance plotted against voltage reveals no difference in somatic Na^+ current density of WT (black; $n = 16$ cells from $N = 3$ mice) and *Scn1a* +/− (blue; $n = 19$ cells from $N = 3$ mice) Ndnf-INs from P16–21 *Scn1a*+/− mice. ***F***, Summary data for maximum peak current density from Ndnf-INs from P16–21 WT versus *Scn1a* +/− mice. ***G***, Voltage dependence of activation of somatic Na^+ currents of Ndnf-INs from WT (black) versus *Scn1a*+/− (blue) mice. All error bars indicate standard error of the mean.

proper subcellular localization (Leterrier et al., 2010; Solé and Tamkun, 2019).

Limitations

There were no differences in the electrophysiological properties of Ndnf-INs between WT and *Scn1a*+/− mice at either P16–21 or P35–56 (Tables 1–4; Figs. 1, 3). We did, however, find subtle differences between Ndnf-IN subclasses in a small subset of selected individual parameters (Tables 1–4; Figs. 2, 4). For example, we found a prolonged AP rise time (0.56 ± 0.02 vs 0.51 ± 0.01 ms) and lower maximal steady-state FF (78.1 ± 2.5 vs 88.1 ± 2.8 Hz) of *Scn1a*+/− versus WT NGFCs, despite there being no difference across a broad range of other properties known to be influenced by Na^+ current density. In contrast, there were no differences between *Scn1a*+/− and WT Canopy cells at P16–21. We also found an isolated lower maximal rise slope and lower AP peak voltage and amplitude in NGFCs from *Scn1a*+/− versus WT mice at P35–56, again with no other differences across other parameters regulated by Na^+ current density

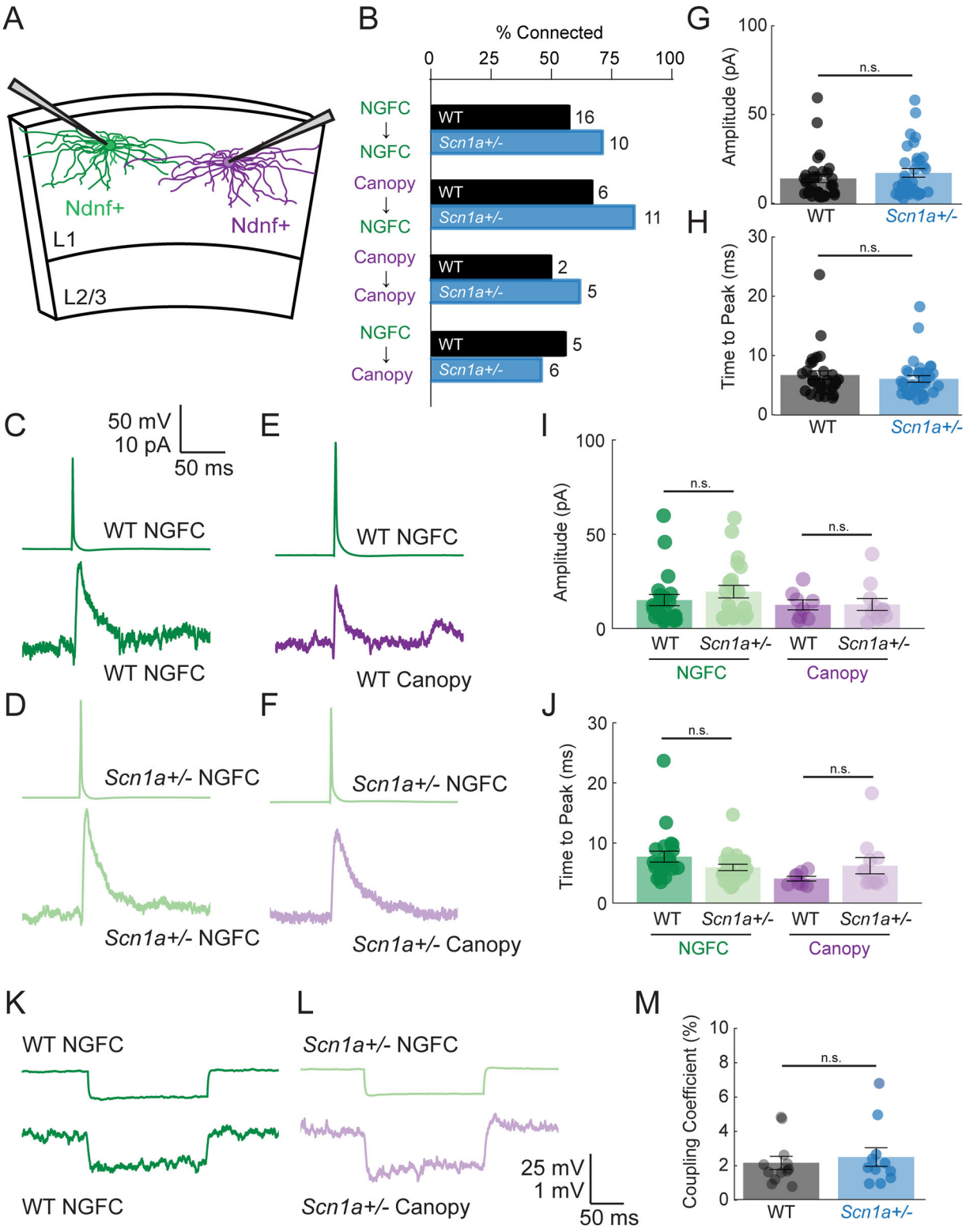

Figure 7. Normal synaptic transmission between Ndnf-INs in *Scn1a*+/− mice. ***A***, Schematic of dual whole-cell patch-clamp recordings of synaptic transmission between Ndnf-INs in Layer 1 primary somatosensory cortex. ***B***, Connection probability for recordings from pairs of Ndnf-INs. Numbers to the right of the bars indicate the number of connected pairs recorded from each combination of cell subpopulations. ***C–F***, Representative traces of evoked unitary IPSCs between (***C***) WT NGFCs, (***D***) *Scn1a*+/− NGFCs, (***E***) a WT presynaptic NGFC and postsynaptic Canopy cell, and (***F***) an *Scn1a*+/− presynaptic NGFC and postsynaptic Canopy cell in P16–21 mice. Postsynaptic cells were held at −50 mV to record outward $GABA_A$ and $GABA_B$ receptor–mediated currents. Traces are the average of 10 trials. Presynaptic cells were stimulated at 0.05 Hz to prevent use-dependent synaptic depression. ***G***, ***H***, Summary data of the (***G***) amplitude and (***H***) time to peak of IPSCs show no differences in WT ($n = 30$ connections from $N = 8$ mice) versus *Scn1a*+/− ($n = 34$ connections from $N = 6$ mice) Ndnf-INs. ***I***, ***J***, Summary data of the (***I***) amplitude and (***J***) time to peak of IPSCs evoked between Ndnf-INs divided on the basis of the firing pattern of the presynaptic cell ($n = 22$ WT NGFC-Ndnf connections; $n = 22$ *Scn1a*+/− NGFC-Ndnf connections; $n = 8$ WT Canopy–Ndnf connections; $n = 11$ *Scn1a*+/− Canopy–Ndnf connections). ***K***, ***L***, Representative traces of electrical connections between Ndnf-INs in WT and *Scn1a*+/− mice during current-clamp recordings in which the presynaptic cell was stimulated with a 100 pA hyperpolarizing current injection. ***M***, Coupling coefficient for electrical connections between Ndnf-INs ($n = 12$ connections from $N = 5$ WT mice; $n = 11$ connections from $N = 2$ *Scn1a*+/− mice). All error bars indicate standard error of the mean.

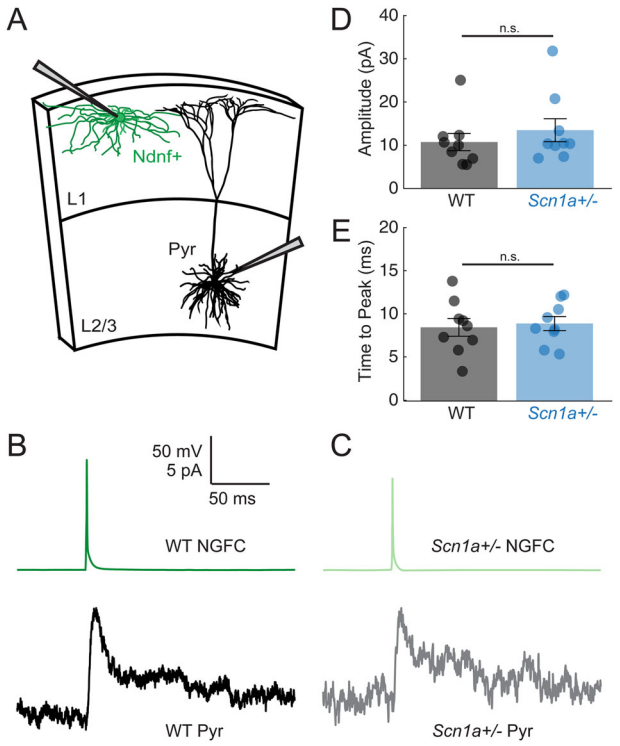

Figure 8. Normal synaptic transmission from Ndnf-INs onto Layer 2/3 pyramidal cells in *Scn1a*+/− mice. ***A***, Schematic of the dual whole-cell patch-clamp recordings of synaptic transmission between Layer 1 Ndnf-INs and Layer 2/3 pyramidal cells in the primary somatosensory cortex. ***B***, ***C***, Representative traces of evoked unitary IPSCs between a presynaptic NGFC and postsynaptic Layer 2/3 pyramidal cell in (***B***) WT and (***C***) *Scn1a*+/− P16–21 mice. Pyramidal cells were held at −50 mV to record outward $GABA_A$ and $GABA_B$ receptor–mediated currents, while Ndnf-INs were stimulated at 0.05 Hz. ***D***, ***E***, Summary data of the (***D***) amplitude and (***E***) time to peak of IPSCs show no differences in WT ($n = 9$ connections from $N = 3$ mice) versus *Scn1a*+/− ($n = 9$ connections from $N = 3$ mice) Ndnf-INs. All error bars indicate standard error of the mean.

and no genotype differences in Canopy cells. The potential physiological relevance of such small differences is unclear. Such data could suggest low-level expression of Nav1.1 in NGFCs that is below the detection threshold of our immunohistochemical assay or outside-out macropatch recordings (which do not sample AIS Na^+ channels). Another possibility is that such differences are due to non–cell-autonomous circuit effects such as differences in baseline synaptic activity (which can influence passive membrane properties and which were not blocked pharmacologically) or changes in K^+ or other ion channels in NGFCs from *Scn1a*+/− mice.

To account for the heterogeneity within the Ndnf-expressing IN subclass, we divided Ndnf-INs into NGFCs and Canopy cells as defined in Schuman et al. (2019) to facilitate analysis of our recordings of intrinsic properties and synaptic transmission. Notably, we were not able to determine the subpopulation identity (NGFC vs Canopy) of individual cells in all experiments, including immunohistochemistry assays, nucleated macropatch recordings, and in vivo 2P calcium imaging. It is possible that future work could employ a combinatorial genetic approach, for instance, crossing *Scn1a*.Ndnf-Flp mice to an Npy-hrGFP line (van den Pol et al., 2009). However, there are multiple confounding variables that may preclude the use of Npy as an effective marker gene, particularly the finding that Npy expression is activity-dependent and is markedly increased after seizures (Wahlestedt et al., 1990; Sperk et al., 1992; Fetissov et al., 2003; Dubé, 2007).

Further investigation is needed to identify the exact voltage-gated Na^+ channels underlying Ndnf-IN excitability in different subcellular compartments. Though our nucleated macropatch recordings allow high-quality, detailed recordings of Na^+ current, it is challenging to determine the exact repertoire of Na^+ channel α subunits that underlie this current without subunit-specific pharmacologic blockers. Direct recordings of axonal Na^+ current (such as at the AIS or branch points) are extremely challenging, have only been performed in INs by a small number of labs, and have never been performed in Ndnf-INs; however, these subcellular compartments likely contain the highest density of Na^+ channels and hence would be expected to exhibit the greatest effect of Na^+ channel haploinsufficiency. Previous work in our lab has indirectly assessed the effects of loss of Nav1.1 in PV-INs by measuring use-/frequency-dependent failures of synaptic transmission (Kaneko et al., 2022). However, unique features of Ndnf-IN–mediated synaptic transmission make it difficult to assess any impact of loss of Na^+ channels on AP propagation in Ndnf-INs using an equivalent paradigm. Ndnf-IN–mediated dendritic IPSCs are much smaller in amplitude and have slower decay kinetics than PV-IN–mediated perisomatic IPSCs (Oláh, 2007; Overstreet-Wadiche and McBain, 2015). As such, it is not possible to classify distinct synaptic events at the IPSC frequencies required to evoke failures in synaptic transmission in PV-INs. Furthermore, Ndnf-IN–mediated IPSCs display significant use-dependent depression, which limits the assessment of synaptic fidelity at rates >0.05 Hz, even in WT Ndnf-INs (Price, 2005). Nevertheless, the lack of significant differences in IPSC amplitude and time to peak of the IPSC in *Scn1a*+/− versus WT Ndnf-INs suggest that there are no dramatic changes in spike propagation or in the number of synaptic contacts made by *Scn1a*+/− Ndnf-INs, both of which are altered in *Scn1a*+/− PV-INs (Kaneko et al., 2022).

Our in vivo recordings suggest that, even within pathological microcircuits in *Scn1a*+/− mice, Ndnf-IN recruitment during arousal is unchanged. It is important to note, however, that we did not explore the complete behavioral parameter space across which Ndnf-IN activity may be recruited. Consequently, we may not have recorded in vivo Ndnf-IN activity in an appropriate behavioral context that would reveal physiologically relevant Ndnf-IN dysfunction, such as the relationship of Ndnf-IN activity to seizures. Though recent studies have reported that Ndnf-INs are recruited in response to auditory and visual stimuli, it is unclear to what degree this sensory-evoked activity can be dissociated from their response to arousal (Abs et al., 2018; Cohen-Kashi Malina et al., 2021). Further work is required to better characterize the circuit function of Layer 1 Ndnf-INs in behaving WT mice to facilitate assessment of Ndnf-IN function or dysfunction in models of disease.

Conclusion

We have identified Layer 1 Ndnf-INs as a subclass unique among neocortical INs in that they do not express Nav1.1 at the AIS or rely on the expression of Nav1.1 for spike generation. As such, neocortical Ndnf-IN intrinsic excitability, synaptic transmission, and circuit function are spared from impairment in an *Scn1a*+/− haploinsufficiency mouse model of DS. This study highlights the importance of neuronal cell-type diversity in a complete mechanistic understanding of neurodevelopmental disorders and in the emerging efforts to develop targeted therapies.

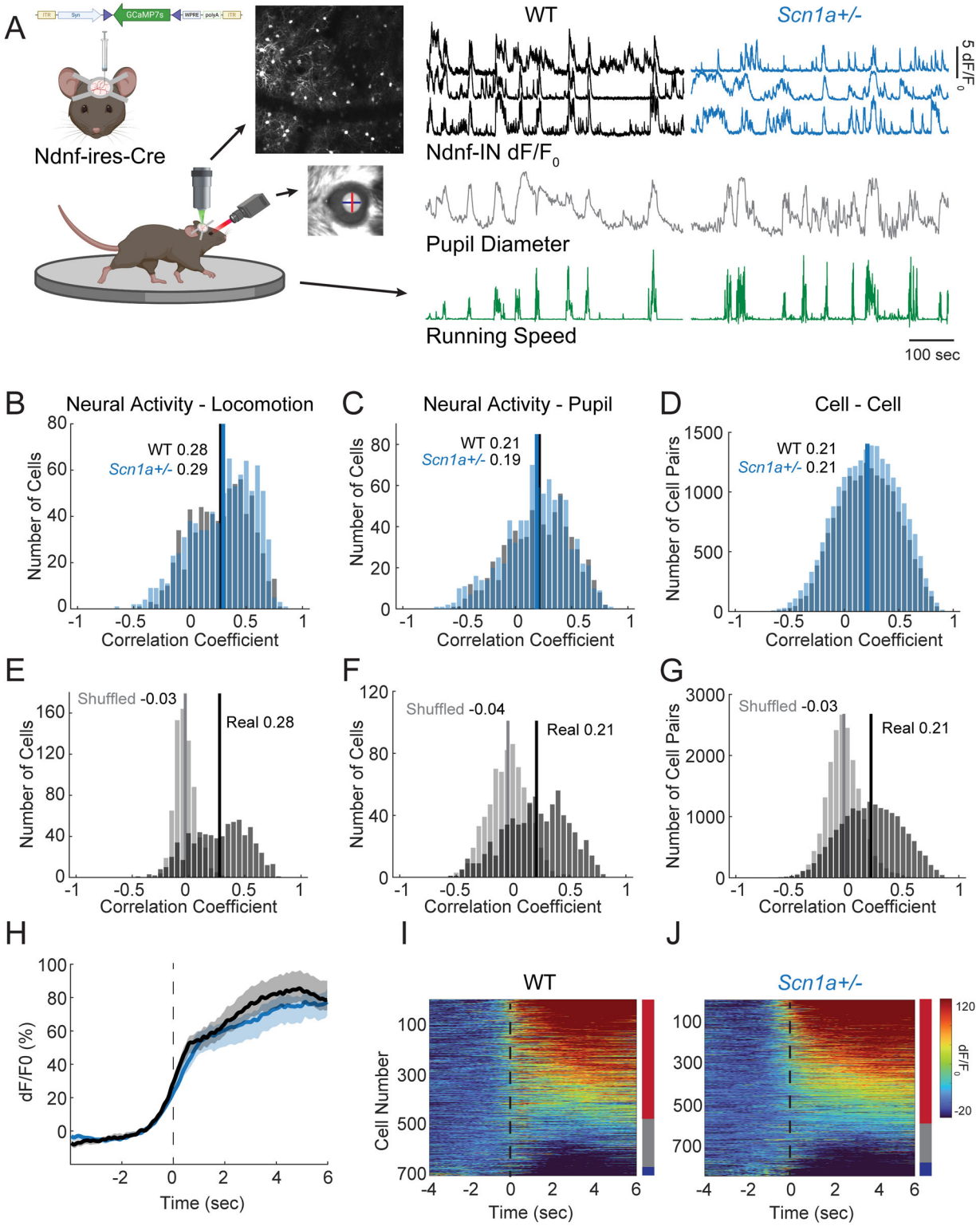

Figure 9. In vivo recruitment of Ndnf-INs during high arousal states is unchanged in *Scn1a*+/− mice relative to WT controls. ***A***, Schematic for in vivo two-photon calcium imaging of Ndnf-INs in awake, behaving head-fixed mice with simultaneous recordings of pupil diameter and locomotion speed. ***B***, Histogram of zero-lag Pearson's correlation coefficients between the dF/F_0 trace and locomotion speed trace for each Ndnf-IN in WT (black; $n = 711$ cells from 4 mice) and *Scn1a*+/− (blue; $n = 844$ cells from 5 mice) littermate controls. Vertical lines and text indicate mean values; $p = 0.04$, Wilcoxon rank sum test. ***C***, Histogram of zero-lag Pearson's correlation coefficients between the dF/F_0 trace and pupil diameter trace for each Ndnf-IN in WT (black) and *Scn1a*+/− (blue) mice. Vertical lines and text indicate mean values; $p = 0.31$, Wilcoxon rank sum test. ***D***, Histogram of the pairwise linear correlation coefficients for the dF/F_0 traces of all pairs of Ndnf-INs in a given FOV. Vertical lines and text indicate mean values; $p = 0.10$, Wilcoxon rank sum test. ***E***, Histogram of zero-lag Pearson's correlation coefficients between the dF/F_0 trace and locomotion speed trace for each Ndnf-IN in WT real and shuffled data. Vertical lines and text indicate mean values; $p = 3.5 \times 10^{-117}$, Wilcoxon rank sum test. ***F***, Histogram of zero-lag Pearson's correlation coefficients between the dF/F_0 trace and pupil diameter trace for each Ndnf-IN in WT real and shuffled data. Vertical lines and text indicate mean values; $p = 1.6 \times 10^{-70}$, Wilcoxon rank sum test. ***G***, Histogram of pairwise linear correlation coefficients for the dF/F_0 traces of all pairs of Ndnf-INs in a given FOV in WT real and shuffled data. Vertical lines and text indicate mean values; $p < 4.9 \times 10^{-324}$, Wilcoxon rank sum test. ***H***, Mean change in dF/F_0 values for all Ndnf-INs aligned to the onset of locomotion in WT (black) and *Scn1a*+/− (blue) age-matched littermates. The shaded regions indicate the 95% bootstrapped CIs. ***I***, ***J***, Heatmaps of mean change in dF/F_0 values for each Ndnf-IN aligned to the onset of locomotion in (***I***) WT age-matched littermates and (***J***) *Scn1a*+/− mice. The side bars indicate the percentage of positive responders (red; WT = 67.9%, *Scn1a*+/− = 70.9%; $p = 0.22$, Fisher's exact test), nonresponders (gray; WT = 27.3%, *Scn1a*+/− = 21.6%), and negative responders (blue; WT = 4.8%, *Scn1a*+/− = 7.6%).

References

Abs E, et al. (2018) Learning-related plasticity in dendrite-targeting layer 1 interneurons. Neuron 100:684–699.e6.

Anastasiades PG, Collins DP, Carter AG (2021) Mediodorsal and ventromedial thalamus engage distinct L1 circuits in the prefrontal cortex. Neuron 109:314–330.e4.

Arshadi C, Günther U, Eddison M, Harrington KIS, Ferreira TA (2021) SNT: a unifying toolbox for quantification of neuronal anatomy. Nat Methods 18:374–377.

Brombas A, Fletcher LN, Williams SR (2014) Activity-dependent modulation of layer 1 inhibitory neocortical circuits by acetylcholine. J Neurosci 34: 1932–1941.

Catterall WA (2018) Dravet syndrome: a sodium channel interneuronopathy. Curr Opin Physiol 2:42–50.

Cauli B (2010) Revisiting the role of neurons in neurovascular coupling. Front Neuroenergetics 2:9.

Cauli B, Tong XK, Rancillac A, Serluca N, Lambolez B, Rossier J, Hamel E (2004) Cortical GABA interneurons in neurovascular coupling: relays for subcortical vasoactive pathways. J Neurosci 24:8940–8949.

Cheah CS, Yu FH, Westenbroek RE, Kalume FK, Oakley JC, Potter GB, Rubenstein JL, Catterall WA (2012) Specific deletion of $Na_V1.1$ sodium channels in inhibitory interneurons causes seizures and premature death in a mouse model of Dravet syndrome. Proc Natl Acad Sci U S A 109: 14646–14651.

Chittajallu R, Auville K, Mahadevan V, Lai M, Hunt S, Calvigioni D, Pelkey KA, Zaghloul KA, McBain CJ (2020) Activity-dependent tuning of intrinsic excitability in mouse and human neurogliaform cells. Elife 9:e57571.

Claes L, Del-Favero J, Ceulemans B, Lagae L, Van Broeckhoven C, De Jonghe P (2001) De novo mutations in the sodium-channel gene SCN1A cause severe myoclonic epilepsy of infancy. Am J Hum Genet 68:1327–1332.

Cohen-Kashi Malina K, et al. (2021) NDNF interneurons in layer 1 gain-modulate whole cortical columns according to an animal's behavioral state. Neuron 109:2150–2164.e5.

Cousin MA, et al. (2021) Pathogenic SPTBN1 variants cause an autosomal dominant neurodevelopmental syndrome. Nat Genet 53:1006–1021.

Csajbók ÉA, et al. (2019) Expression of GLP-1 receptors in insulin-containing interneurons of rat cerebral cortex. Diabetologia 62:717–725.

Dravet C (2011) Dravet syndrome history. Dev Med Child Neurol 53:1–6.

Dubé C (2007) Neuropeptide Y: potential role in recurrent developmental seizures. Peptides 28:441–446.

Duflocq A, Le Bras B, Bullier E, Couraud F, Davenne M (2008) Nav1.1 is predominantly expressed in nodes of Ranvier and axon initial segments. Mol Cell Neurosci 39:180–192.

Favero M, Sotuyo NP, Lopez E, Kearney JA, Goldberg EM (2018) A transient developmental window of fast-spiking interneuron dysfunction in a mouse model of Dravet syndrome. J Neurosci 38:7912–7927.

Fetissov SO, Jacoby AS, Brumovsky PR, Shine J, Iismaa TP, Hökfelt T (2003) Altered hippocampal expression of neuropeptides in seizure-prone GALR1 knockout mice. Epilepsia 44:1022–1033.

Goff KM, Goldberg EM (2019) Vasoactive intestinal peptide-expressing interneurons are impaired in a mouse model of Dravet syndrome. Elife 8: e46846.

Goff KM, Liebergall SR, Jiang E, Somarowthu A, Goldberg EM (2023) VIP interneuron impairment promotes in vivo circuit dysfunction and autism-related behaviors in Dravet syndrome. Cell Rep 42:112628.

Gouwens NW, et al. (2020) Integrated morphoelectric and transcriptomic classification of cortical GABAergic cells. Cell 183:935–953.e19.

Han S, Tai C, Westenbroek RE, Yu FH, Cheah CS, Potter GB, Rubenstein JL, Scheuer T, de la Iglesia HO, Catterall WA (2012) Autistic-like behaviour in Scn1a+/− mice and rescue by enhanced GABA-mediated neurotransmission. Nature 489:385–390.

Hay YA, Deperrois N, Fuchsberger T, Quarrell TM, Koerling A-L, Paulsen O (2021) Thalamus mediates neocortical down state transition via GABAB-receptor-targeting interneurons. Neuron 109:2682–2690.e5.

Hu W, Tian C, Li T, Yang M, Hou H, Shu Y (2009) Distinct contributions of Nav1.6 and Nav1.2 in action potential initiation and backpropagation. Nat Neurosci 12:996–1002.

Jiang X, Wang G, Lee AJ, Stornetta RL, Zhu JJ (2013) The organization of two new cortical interneuronal circuits. Nat Neurosci 16:210–218.

Kaneko K, Currin CB, Goff KM, Wengert ER, Somarowthu A, Vogels TP, Goldberg EM (2022) Developmentally regulated impairment of parvalbumin interneuron synaptic transmission in an experimental model of Dravet syndrome. Cell Rep 38:110580.

Kawaguchi Y (1995) Physiological subgroups of nonpyramidal cells with specific morphological characteristics in layer II/III of rat frontal cortex. J Neurosci 15:2638–2655.

Kim J-Y, Ash RT, Ceballos-Diaz C, Levites Y, Golde TE, Smirnakis SM, Jankowsky JL (2013) Viral transduction of the neonatal brain delivers controllable genetic mosaicism for visualising and manipulating neuronal circuits in vivo. Eur J Neurosci 37:1203–1220.

Kole MHP, Ilschner SU, Kampa BM, Williams SR, Ruben PC, Stuart GJ (2008) Action potential generation requires a high sodium channel density in the axon initial segment. Nat Neurosci 11:178–186.

Leterrier C, Brachet A, Fache M-P, Dargent B (2010) Voltage-gated sodium channel organization in neurons: protein interactions and trafficking pathways. Neurosci Lett 486:92–100.

Lorenzo DN, Badea A, Zhou R, Mohler PJ, Zhuang X, Bennett V (2019) βII-spectrin promotes mouse brain connectivity through stabilizing axonal plasma membranes and enabling axonal organelle transport. Proc Natl Acad Sci U S A 116:15686–15695.

Lorincz A, Nusser Z (2008) Cell-type-dependent molecular composition of the axon initial segment. J Neurosci 28:14329–14340.

Lorincz A, Nusser Z (2010) Molecular identity of dendritic voltage-gated sodium channels. Science 328:906–909.

Meng JH, Schuman B, Rudy B, Wang X-J (2023) Mechanisms of dominant electrophysiological features of four subtypes of layer 1 interneurons. J Neurosci 43:3202–3218.

Miller AR, Hawkins NA, McCollom CE, Kearney JA (2014) Mapping genetic modifiers of survival in a mouse model of Dravet syndrome: genetic modifiers of Dravet syndrome. Genes Brain Behav 13:163–172.

Mistry AM, Thompson CH, Miller AR, Vanoye CG, George AL, Kearney JA (2014) Strain- and age-dependent hippocampal neuron sodium currents correlate with epilepsy severity in Dravet syndrome mice. Neurobiol Dis 65:1–11.

Molnár G, et al. (2014) GABAergic neurogliaform cells represent local sources of insulin in the cerebral cortex. J Neurosci 34:1133–1137.

Muralidhar S, Wang Y, Markram H (2014) Synaptic and cellular organization of layer 1 of the developing rat somatosensory cortex. Front Neuroanat 7:52.

Ogiwara I, et al. (2007) Nav1.1 localizes to axons of parvalbumin-positive inhibitory interneurons: a circuit basis for epileptic seizures in mice carrying an Scn1a gene mutation. J Neurosci 27:5903–5914.

Oláh S (2007) Output of neurogliaform cells to various neuron types in the human and rat cerebral cortex. Front Neural Circuits 1:4.

Onwuli DO, Beltran-Alvarez P (2016) An update on transcriptional and post-translational regulation of brain voltage-gated sodium channels. Amino Acids 48:641–651.

Overstreet-Wadiche L, McBain CJ (2015) Neurogliaform cells in cortical circuits. Nat Rev Neurosci 16:458–468.

Pachitariu M, Stringer C, Dipoppa M, Schröder S, Rossi LF, Dalgleish H, Carandini M, Harris KD (2016) Suite2p: beyond 10,000 neurons with standard two-photon microscopy. bioRxiv 29:1–3.

Poorthuis RB, Muhammad K, Wang M, Verhoog MB, Junek S, Wrana A, Mansvelder HD, Letzkus JJ (2018) Rapid neuromodulation of layer 1 interneurons in human neocortex. Cell Rep 23:951–958.

Price CJ (2005) Neurogliaform neurons form a novel inhibitory network in the hippocampal CA1 area. J Neurosci 25:6775–6786.

Ramon y Cajal S (1922) Studien über die Sehrinde der Katze. J Neurol Psychiatry 29:161–181.

Rubinstein M, Han S, Tai C, Westenbroek RE, Hunker A, Scheuer T, Catterall WA (2015) Dissecting the phenotypes of Dravet syndrome by gene deletion. Brain 138:2219–2233.

Schindelin J, et al. (2012) Fiji: an open-source platform for biological-image analysis. Nat Methods 9:676–682.

Schuman B, Dellal S, Prönneke A, MacHold R, Rudy B (2021) Neocortical layer 1: an elegant solution to top-down and bottom-up integration. Annu Rev Neurosci 44:221–252.

Schuman B, Machold RP, Hashikawa Y, Fuzik J, Fishell GJ, Rudy B (2019) Four unique interneuron populations reside in neocortical layer 1. J Neurosci 39:125–139.

Solé L, Tamkun MM (2019) Trafficking mechanisms underlying Nav channel subcellular localization in neurons. Channels 14:1–17.

Sperk G, Marksteiner J, Gruber B, Bellmann R, Mahata M, Ortler M (1992) Functional changes in neuropeptide Y- and somatostatin-containing neurons induced by limbic seizures in the rat. Neuroscience 50:831–846.

Tai C, Abe Y, Westenbroek RE, Scheuer T, Catterall WA (2014) Impaired excitability of somatostatin- and parvalbumin-expressing cortical interneurons in a mouse model of Dravet syndrome. Proc Natl Acad Sci U S A 111:E3139–E3148.

Tamagnini F (2021) Nucleated, outside-out, somatic, macropatch recordings in native neurons. In: *Patch clamp electrophysiology: methods and protocols* (Dallas M, Bell D, eds), pp 229–242. New York, NY: Springer US; Methods in Molecular Biology.

Tamás G, Lörincz A, Simon A, Szabadics J (2003) Identified sources and targets of slow inhibition in the neocortex. Science 299:1902–1905.

Tasic B, et al. (2016) Adult mouse cortical cell taxonomy revealed by single cell transcriptomics. Nat Neurosci 19:335–346.

Tran CH, Vaiana M, Nakuci J, Somarowthu A, Goff KM, Goldstein N, Murthy P, Muldoon SF, Goldberg EM (2020) Interneuron desynchronization precedes seizures in a mouse model of Dravet syndrome. J Neurosci 40:2764–2775.

Tremblay R, Lee S, Rudy B (2016) GABAergic interneurons in the neocortex: from cellular properties to circuits. Neuron 91:260–292.

van den Pol AN, Yao Y, Fu L-Y, Foo K, Huang H, Coppari R, Lowell BB, Broberger C (2009) Neuromedin B and gastrin-releasing peptide excite arcuate nucleus neuropeptide Y neurons in a novel transgenic mouse expressing strong Renilla green fluorescent protein in NPY neurons. J Neurosci 29:4622–4639.

Wahlestedt C, Blendy JA, Kellar KJ, Heilig M, Widerlöv E, Ekman R (1990) Electroconvulsive shocks increase the concentration of neocortical and hippocampal neuropeptide Y (NPY)-like immunoreactivity in the rat. Brain Res 507:65–68.

Wozny C, Williams SR (2011) Specificity of synaptic connectivity between layer 1 inhibitory interneurons and layer 2/3 pyramidal neurons in the rat neocortex. Cereb Cortex 21:1818–1826.

Yao Z, et al. (2021) A taxonomy of transcriptomic cell types across the isocortex and hippocampal formation. Cell 184:3222–3241.e26.

Yu FH, Mantegazza M, Westenbroek RE, Robbins CA, Kalume F, Burton KA, Spain WJ, McKnight GS, Scheuer T, Catterall WA (2006) Reduced sodium current in GABAergic interneurons in a mouse model of severe myoclonic epilepsy in infancy. Nat Neurosci 9:1142–1149.

Zhu Y, Zhu JJ (2004) Rapid arrival and integration of ascending sensory information in layer 1 nonpyramidal neurons and tuft dendrites of layer 5 pyramidal neurons of the neocortex. J Neurosci 24:1272–1279.